Tropical Cyclone Forecasts Impact Assessment from the Assimilation of Hourly Visible, Shortwave, and Clear-Air Water Vapor Atmospheric Motion Vectors in HWRF

AGNES H. N. LIM, JAMES A. JUNG, AND SHARON E. NEBUDA

Cooperative Institute for Meteorological Satellite Studies, University of Wisconsin–Madison, Madison, Wisconsin

JAIME M. DANIELS

NOAA/NESDIS/Center for Satellite Applications and Research, Camp Springs, Maryland

WAYNE BRESKY

NOAA/NESDIS/Center for Satellite Applications and Research, Camp Springs, and I.M. Systems Group, Rockville, Maryland

MINGJING TONG

NOAA/NWS/NCEP/Environmental Modeling Center, College Park, and I.M. Systems Group, Rockville, Maryland

VIJAY TALLAPRAGADA

NOAA/NWS/NCEP/Environmental Modeling Center, College Park, Maryland

ABSTRACT

The assimilation of atmospheric motion vectors (AMVs) provides important wind information to conventional data-lacking oceanic regions, where tropical cyclones spend most of their lifetimes. Three new AMV types, shortwave infrared (SWIR), clear-air water vapor (CAWV), and visible (VIS), are produced hourly by NOAA/NESDIS and are assimilated in operational NWP systems. The new AMV data types are added to the hourly infrared (IR) and cloud-top water vapor (CTWV) AMV data in the 2016 operational version of the HWRF Model. In this study, we update existing quality control (QC) procedures and add new procedures specific to tropical cyclone assimilation. We assess the impact of the three new AMV types on tropical cyclone forecasts by conducting assimilation experiments for 25 Atlantic tropical cyclones from the 2015 and 2016 hurricane seasons. Forecasts are analyzed by considering all tropical cyclones as a group and classifying them into strong/weak storm vortices based on their initial model intensity. Metrics such as track error, intensity error, minimum central pressure error, and storm size are used to assess the data impact from the addition of the three new AMV types. Positive impact is obtained for these metrics, indicating that assimilating SWIR-, CAWV-, and VIS-type AMVs are beneficial for tropical cyclone forecasting. Given the results presented here, the new AMV types were accepted into NOAA/NCEP's operational HWRF for the 2017 hurricane season.

1. Introduction

The National Hurricane Center's (NHC) yearly mean absolute error plots for different forecast hours of track and intensity show substantial improvement in tropical cyclone (TC) track forecast error over the last 20 years, with 72-h track errors being reduced by half (Cangialosi and Franklin 2017; their Figs. 3 and 9). This improvement is attributed to better global analyses and forecasts as the tropical cyclone track is mostly determined by large-scale environmental flow. However, in the case of intensity, improvements in forecast skill have been smaller. Forecast skill of intensity is largely driven by the fact that tropical cyclone intensity is dependent on the accuracy of modeling and observing storm-scale processes especially in the inner core of the storm.

Corresponding author: Agnes H. N. Lim, alim@ssec.wisc.edu

Forecasting tropical cyclones requires adequate modeling of the dynamical and physical processes to simulate the growth and decay of the TC through its lifespan. A good representation of the tropical cyclone's atmospheric state and nearby environment are also needed to correctly simulate the interaction between the storm and its environment. The value of wind measurements in tropical cyclone forecasting was demonstrated with the inclusion of dropwindsonde observations. Aberson and Franklin (1999), Aberson (2011), Chou et al. (2011), and Christophersen et al. (2018) showed that the assimilation of dropwindsonde data provided significant improvements in the forecast TC track and intensity. They also found evidence that synoptic-scale observations in the upper troposphere were related to the improvement in TC intensity forecasts.

Historically, direct observation of the vector wind field has been provided by conventional data (e.g., rawinsondes). These observations, however, are unevenly distributed and often concentrated over land. The lack of conventional observations in the tropical oceans where tropical cyclones begin and spend most of their life is mitigated by the existence and use of satellite observations. Today's data assimilation systems used to forecast these tropical cyclones rely heavily on satellites to provide the majority of the observations. The need for a better representation of the analyzed TC environment and surrounding synoptic circulation motivates the use of derived satellite wind products to fill this data void.

One type of satellite wind product is the atmospheric motion vectors (AMVs). The AMVs are derived by tracking the horizontal motion of atmospheric fields such as clouds or water vapor gradients from consecutive satellite images taken 30 minutes apart (Menzel 2001). Both polar-orbiting and geostationary satellites use this technique to derive AMVs. Geostationary satellites are able to generate AMVs at higher temporal resolution than polar satellites due to their orbital and scanning geometry (Velden et al. 2005). Numerical weather prediction (NWP) centers such as the European Centre for Medium-Range Weather Forecasts (ECMWF), the Met Office, the Bureau of Meteorology (BoM), the Korea Meteorological Agency (KMA), and the National Centers for Environmental Prediction (NCEP) have switched from AMVs generated once every 6 h to using hourly generated AMVs in their global and/or regional models after showing improved forecast skill (Bormann et al. 2012; Cotton and Forsythe 2012; Le Marshall et al. 2013; Lee et al. 2012; Su et al. 2014).

The abundance of high temporal and high spatial resolution satellite AMVs in the tropics is especially beneficial around tropical cyclones. Le Marshall and Leslie (1999) showed that analyses and intensity forecasts of tropical cyclones had improved from the assimilation of these AMVs, most notably in the upper outflow regions. Hourly AMV assimilation studies conducted by the U.S. Navy, using the Navy Operational Global Atmospheric Prediction System (NOGAPS) (Bayler and Lewit 1992), showed positive impacts in tropical cyclone track forecasts (Langland et al. 2009; Goerss 2009; Berger et al. 2011). Using a larger sample size (50 cases in 2005 and 26 cases in 2006), Goerss (2009) arrived at a similar conclusion. Goerss (2009) found that the improvement in TC track forecasts ranged from 7% to 24%, and were statistically significant at all forecast lengths. For tropical cyclones in the Coral Sea and the Atlantic Ocean, the benefits of hourly cloud-drift winds from *GOES-8* and *Geostationary Meteorological Satellite-5* (*GMS-5*) were explored using different assimilation techniques conducted within a limited-area model (Le Marshall et al. 1996a,b,c; Leslie et al. 1998; Le Marshall and Leslie 1999). The results indicated that assimilating hourly AMVs using variational assimilation techniques showed a 100–200-km reduction in tropical cyclone mean track errors. Due to the positive impact on tropical cyclone forecasts from assimilating hourly AMVs, the goal of this work is to expand the NCEP Hurricane and Weather Forecast (HWRF) system to assimilate all five types of hourly AMVs for operational tropical cyclone forecasting.

The paper is organized as follows. Section 2 provides a summary of the AMVs used in this study and the 2016 HWRF system. Section 3a describes the new quality control procedures and experimental design to assess the impact of the new data types. In section 3b, a single assimilation cycle is reviewed to demonstrate that the analysis increments of the new AMV types are consistent with the current AMV types in the HWRF system. Section 4a discusses the results of the forecast performance for all tropical cyclones during the 2015 and 2016 hurricane seasons. Forecast performance resulting from the assimilation of the new hourly AMV types for strong and weak storm vortices is examined in section 4b. Section 5 gives a summary of the findings and future plans.

2. Background

a. GOES AMVs

The National Oceanic and Atmospheric Administration's (NOAA) National Environmental Satellite, Data, and Information Service (NESDIS) routinely generates hourly AMVs from the GOES-East and West satellites for use by NWP. Five types of AMVs are derived from the geostationary images: shortwave infrared (SWIR),

TABLE 1. GOES imager spectral channels used to derive the different AMV types.

Types of AMVs	GOES spectral channel use
Visible (VIS)	Channel 1: 0.68 μm
Shortwave infrared (SWIR)	Channel 2: 3.9 μm
Cloud-top water vapor	Channel 3: 6.9 μm
Clear-air water vapor	
Infrared	Channel 4: 10.7 μm

infrared (IR), cloud-top water vapor (CTWV), clear air water vapor (CAWV), and visible (VIS). The GOES spectral channels that are used to derive the different AMV types are listed in Table 1. SWIR- and VIS-type AMVs are located in the lower troposphere between 700 and 1000 hPa, whereas the CTWV- and CAWV-type AMVs reside predominantly in the upper troposphere, between 100 and 400 hPa. The IR-type AMVs are predominantly below 800 hPa and above 400 hPa. AMV wind speeds in the upper troposphere are faster than those lower in the troposphere (Fig. 1). Coverage of VIS- and SWIR-type AMVs are complementary due to their diurnal patterns. VIS-type AMVs are available during daylight hours; the SWIR-type AMVs are available at night.

Two inputs are required to derive GOES AMVs, three-time-sequence satellite images (triplet) and model wind field forecasts valid at the time of the images. The model forecast lengths are limited to within 9 h from the time of the first satellite image of the triplet. The satellite images are checked and corrected for navigation shifts between the set of images using predetermined landmark points. Suitable tracer or vector targets are then identified. These targets can be cloud edges, defined cloud features, or gradients of water vapor. Cross correlations are used to track the displacements of identified targets in the triplets with guidance from the model forecast wind field. Potential height assignment values are then calculated for each target scene using any or all four of the following methods: the infrared window channel, the water vapor histogram method, the water vapor infrared window intercept method, and the CO_2–infrared window ratio method (Nieman et al. 1997). These potential heights are determined by comparing simulated brightness temperatures from Global Forecast System (GFS) model first-guess values with that from the observed. A "best" height assignment value, as defined by the data provider, is then selected from the four values depending on the satellite channel used for the tracked images. The derived wind vectors are then subjected to editing and quality control by NESDIS. The current GOES AMVs have a height reassignment routine called the Auto-Editor. The wind
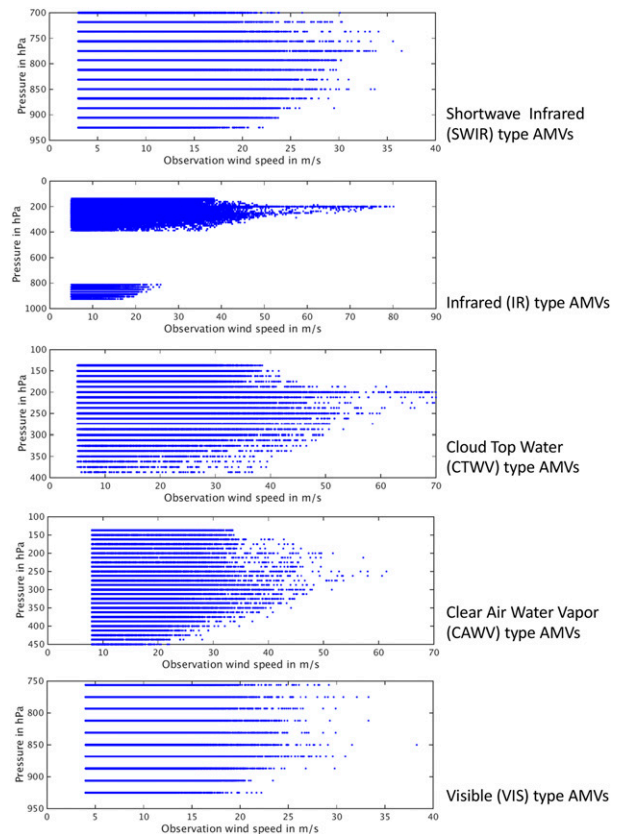

FIG. 1. Distribution of the different types of AMVs in the atmosphere.

vector editor will examine the initial wind vector height assignment and possibly reassign it with a value that is derived from a variational penalty function (Velden et al. 1997), which has a dependency on model forecast wind, temperature, and pressure fields.

b. HWRF system

The HWRF is an atmosphere–ocean coupled system dedicated to tropical cyclone application. Initial and boundary conditions of the parent domain are provided by the NCEP GFS analysis. The HWRF employs physical parameterization suite suitable for tropical cyclone applications. The parameterizations are the GFDL surface-layer parameterization, the Noah land surface model (LSM; Chen and Dudhia 2001; Mitchell 2005), the Rapid Radiative Transfer Model for general circulation models radiation scheme (RRTMG; Iacono et al. 2008), the Ferrier–Aligo microphysics (Rogers et al. 2001; Ferrier et al. 2002), the GFS Hybrid Eddy Diffusivity Mass-Flux (Hybrid-ESMF) planetary boundary layer (PBL) scheme (Gopalakrishnan et al. 2013), and the scale-aware GFS simplified Arakawa–Schubert (SAS) deep and shallow convection scheme
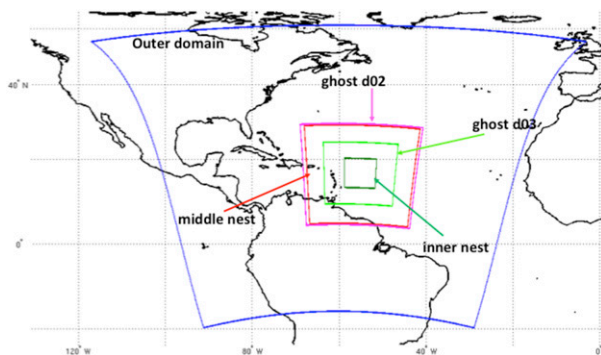
FIG. 2. HWRF data assimilation and forecast domains. The parent domain is $80° \times 80°$ with its center determined based on the initial location of the storm's position and the 72-h forecast from NHC or the JTWC. The two nested domains are $25° \times 25°$ and $8.3° \times 8.3°$. Resolutions of the outer, middle, and inner domains are 18, 6, and 2 km, respectively. Data assimilation is applied to the ghost d02 and d03 domains, and they have the same spatial resolution as the nested domains, but with larger coverage ($28° \times 28°$ and $15° \times 15°$).

(Arakawa and Schubert 1974; Grell 1993). Detailed information on the 2016 HWRF can be found in Biswas et al. (2016a,b).

The HWRF is configured with a parent domain and two storm-following nested domains (Fig. 2). The parent domain is roughly $80° \times 80°$ with its center determined by the initial location of the storm's position and the 72-h forecast from NHC or the Joint Typhoon Warning Center (JTWC). The two nested domains are $25° \times 25°$ and $8.3° \times 8.3°$. Both nested domains are two-way interactive; that is, there is information exchange between the domains and their parent domain. The three domains have spatial resolutions of $0.135°$ ($\sim$18 km), $0.045°$ ($\sim$6 km), and $0.015°$ ($\sim$2 km) (Biswas et al. 2016a). HWRF has two ghost domains used for data assimilation (Tong et al. 2018). They have the same spatial resolution as the nested domains. However, the ghost domains have larger coverage ($28° \times 28°$ and $15° \times 15°$). The ghost d02 domain sufficiently covers the whole storm, while the ghost d03 domain is used primarily to assimilate aircraft reconnaissance data. The HWRF has 61 vertical levels and a model top at 2 hPa. The vertical resolution remains the same for all three domains.

The HWRF Data Assimilation System (HDAS) uses a hybrid three-dimensional (3D) ensemble-variational data assimilation (EnVar) system (Wang et al. 2013) implementation of the Gridpoint Statistical Interpolation (GSI). As the ensembles do not feedback into the next analysis cycle, data assimilation performed on the two ghost domains is termed "one-way hybrid." The first guess used to initialize the HWRF nested domains is the NCEP Global Data Assimilation System (GDAS) 6-h forecast. Prior to data assimilation, the vortex (position, structure, and intensity) in the first guess is modified based on the NHC's Tropical Cyclone Vitals (TC Vitals) database. The vortex to replace the first guess can either be drawn from a HWRF 6-h forecast from an earlier run or the GDAS 6-h forecast. If the observed vortex maximum wind speed is greater or equal to $14 \, \text{m s}^{-1}$ and a previous 6-h HWRF forecast is available, the vortex from the 6-h HWRF forecast is extracted. This vortex is corrected based on NHC's TC Vitals and inserted into the first guess. Otherwise, the corrected vortex from the 6-h GDAS forecast is used. Details on the vortex correction can be found in Biswas et al. (2016b). This vortex-processing step, also known as vortex initialization (Tong et al. 2018), is designed to optimize forecast skill (Lu et al. 2017; Tong et al. 2018), but it can limit the impact of adding new AMV types by inhibiting the propagation of information from observations assimilated in earlier analysis cycles into the current analysis cycle.

The use of a static background error covariance matrix, which is isotropic and constrained by larger-scale geostrophic balance, limits the spreading of observation information in the presence of a TC (Lu et al. 2017; Tong et al. 2018). To provide information on the flow-dependent error covariance for GSI, a 40-member HWRF forecast-based ensemble is used when Tail Doppler Radar (TDR) data are available. In the event where there are no TDR data, the 80-member GFS ensemble is used. Observation types that HDAS assimilates are conventional observations (Table 2), TDR data, satellite infrared and microwave radiances, hourly GOES IR and CTWV-type AMVs, and Global Positioning System (GPS) radio occultation bending angle. Tables 2 and 3 provide a complete list of observations assimilated in HDAS. The HDAS assimilates observations within ± 3 h of the analysis time. Two outer loops with 50 iterations each are used in GSI during the minimization process.

A merging procedure is applied after data assimilation to combine the HDAS analyses to the GDAS analysis, valid at the same time to produce the final analysis. The data are interpolated to the parent and nested domains to generate a final analysis to be used to initialize the HWRF forecast. For TCs with maximum winds greater than 64 kt ($1 \, \text{kt} \approx 0.51 \, \text{m s}^{-1}$), data assimilation increments are excluded within 150 km of the TC center and below 600 hPa. Data assimilation increments are gradually introduced between 150 and 300 km. This exclusion is intended to alleviate spindown problems but removes the impact from assimilation of observations within 150 km of the TC

TABLE 2. Conventional observations used within HDAS where T is temperature, Q is humidity, and Ps is surface pressure.

Instruments	Variables assimilated
Synthetic tropical storm center	Ps
Rawinsonde	T, Q, Ps, and u- and v-component wind
AIREP and PREP pilot report aircraft	T and u- and v-component wind
Aircraft Meteorological Data Relay (AMDAR) aircraft	T and u- and v-component wind
Flight-level reconnaissance and profile dropsonde	T, Q, and u- and v-component wind
Minimum obstruction clearance altitudes (MOCAs) aircraft temperature and humidity	T, Q, u- and v-component wind
Surface marine ship, buoy, and C-MAN temperature, humidity, and surface pressure	T, Q, Ps, and u- and v-component wind
Surface land and METAR	T, Q, Ps, and u- and v-component wind
Splash-level dropsonde	T, Q, and Ps
NEXRAD vertical azimuth display	u- and v-component wind
Pilot balloon (PIBAL)	u- and v-component wind

center. For weak TCs (maximum winds less than 64 kt) data assimilation increments will play a part in correcting the forecasts.

The HWRF system is only run when NHC or JTWC identifies an area or disturbance that has the potential of becoming a tropical depression in their area of responsibility. Once a tropical cyclone is identified, the HWRF is run four times daily to produce 126-h forecasts of TC track, intensity, structure, and rainfall. The HWRF run is terminated when the tropical cyclone either dissipates after making landfall, becomes extratropical, or degenerates into a remnant low. Figure 3 shows a schematic of various processes that take place during an HWRF run during a single analysis time.

Experiments in this study were run with the 2016 version of the operational HWRF/HDAS on the NOAA High Performance Computing cluster JET. The model configuration, runtime scripts, and all data files were provided by NCEP, and experiments were conducted in accordance with NCEP's parallel testing procedures.

3. Data assimilation of SWIR-, CAWV-, and VIS-type AMVs derived from the heritage algorithm

a. Experimental setup, data quality control, and observational error

Two sets of assimilation runs are completed for each tropical cyclone case to evaluate the HWRF performance with the addition of the new GOES AMV types. The control (CTRL) assimilates the whole suite of observations used operationally as described in section 2b. The AMVs types that are assimilated operationally are the hourly IR and CTWV from GOES-East and West. The experiment (AMV1) is identical to the CTRL but with the additional assimilation of hourly SWIR-, CAWV-, and VIS-type AMVs. These AMVs are already present in the NCEP data stream and ready to be used by the assimilation system.

Current quality control (QC) procedures for AMVs assimilated in the GSI are derived for the global model. These QC procedures are based on metrics [AMV location and departure (difference from the model first-guess wind fields)] provided by the data producer.

TABLE 3. Satellite observations used by HDAS.

| Instrument	Variables assimilated
HIRS	IR radiances
Infrared atmospheric sounding interferometer (IASI)	
AIRS	
Cross-Track Infrared Sounder (CrIS)	
SEVIRI	
GOES Sounder	
AMSU-A	Microwave radiances
Microwave Humidity Sounder (MHS)	
SSMIS	
Advanced Technology Microwave Sounder (ATMS)	
Hourly GOES infrared and cloud-top water-vapor-type AMVs	Wind speed and direction
EUMETSAT AMVs	
ASCAT scatterometer winds	
GPS radio occultation	Bending angles
GPS	Integrated precipitable water
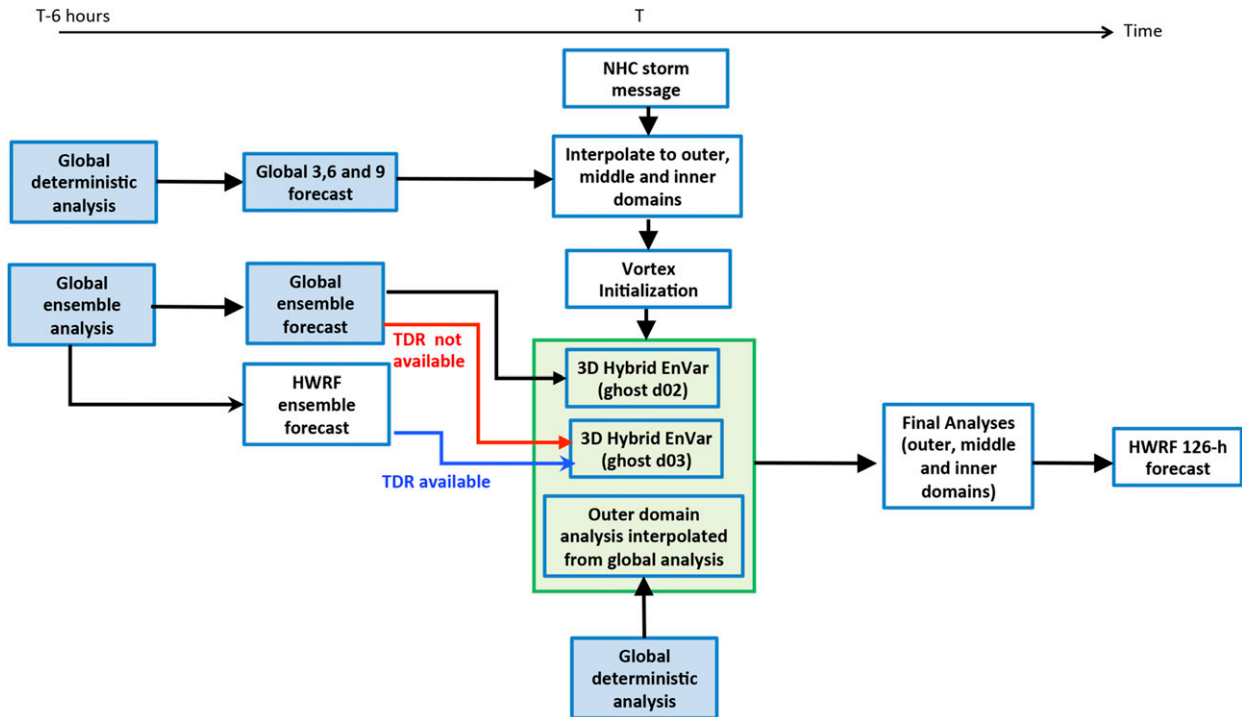
FIG. 3. Flow diagram of a HWRF run at analysis time *T*. Blue-shaded boxes indicate components from NCEP's global system. The tasks enclosed by the green-shaded region indicate how the analysis of each of the HWRF domains is generated.

The SWIR-, IR-, CTWV-, and VIS-type AMVs are used if the assigned quality indicator (QI) (Holmlund 1998) computed without the forecast component is greater than 85. The IR- and CTWV-type AMVs are used if their normalized expected error (EE) (Le Marshall et al. 2004) (EE/AMV speed) is less than $0.8 \, \mathrm{m \, s}^{-1}$. For low-level IR-type AMVs with pressure values larger than 800 hPa, the normalized EE must be less than $0.55 \, \mathrm{m \, s}^{-1}$ to pass QC. All AMV types (SWIR, IR, CTWV, CAWV, and VIS) are subjected to a near-surface and tropopause check. Atmospheric motion vector observations with pressures less than 950 hPa and below the tropopause are used. The IR-type AMV observations over land with latitudes greater than 20°N have been found to be problematic and are rejected. In addition, IR-type AMVs with pressure values between 400 and 800 hPa and CTWV-type AMVs with pressure values greater than 400 hPa are excluded due to height assignment concerns. The CAWV-type AMVs are also rejected if the difference in the wind direction is greater than 50° from the forecast wind.

New HDAS QC checks for SWIR-, CAWV-, and VIS-type AMVs were added to optimize the use of these observations in the HWRF. The low speed threshold of CAWV-type AMVs was reduced from 10 to $8 \, \mathrm{m \, s}^{-1}$. This change increased the number of AMVs considered for assimilation. Statistics of normalized wind speed differences and normalized vector differences

were calculated to investigate the performance of the new QC procedures. Statistics were computed at 50-hPa intervals for SWIR-, CAWV-, and VIS-type AMVs using innovations (observed − first guess) and analysis error (observed − analysis). Figure 4 shows the calculated normalized wind speed differences and normalized vector differences from all 39 assimilation cycles of Hurricane Joaquin. Also plotted in Fig. 4 is the number of observations assimilated with and without the new QC checks for each AMV type to show how these checks influence the total counts. Prior to additional data filtering, large biases in normalized wind speed differences are observed for SWIR-type AMVs with pressures less than 700 hPa, CAWV-type AMVs with pressures greater than 450 hPa, and VIS-type AMVs with pressures less than 750 hPa (orange and green curves in Fig. 4). The large bias may be a result of placing the low-level AMVs at the base of a temperature inversion, as explained by (Heidinger, 2010). Quality control checks to limit AMVs in the vertical extent by rejecting AMVs above–below a set of pressure levels are added to remove observations that contribute to the large biases (red and blue curves in Fig. 4). For SWIR-type AMVs, a minimum pressure is set to 700 hPa and for VIS-type AMVs the minimum pressure is set to 750 hPa. Likewise, CAWV-type AMVs are not used if their pressure values are greater than 450 hPa. These QC procedures
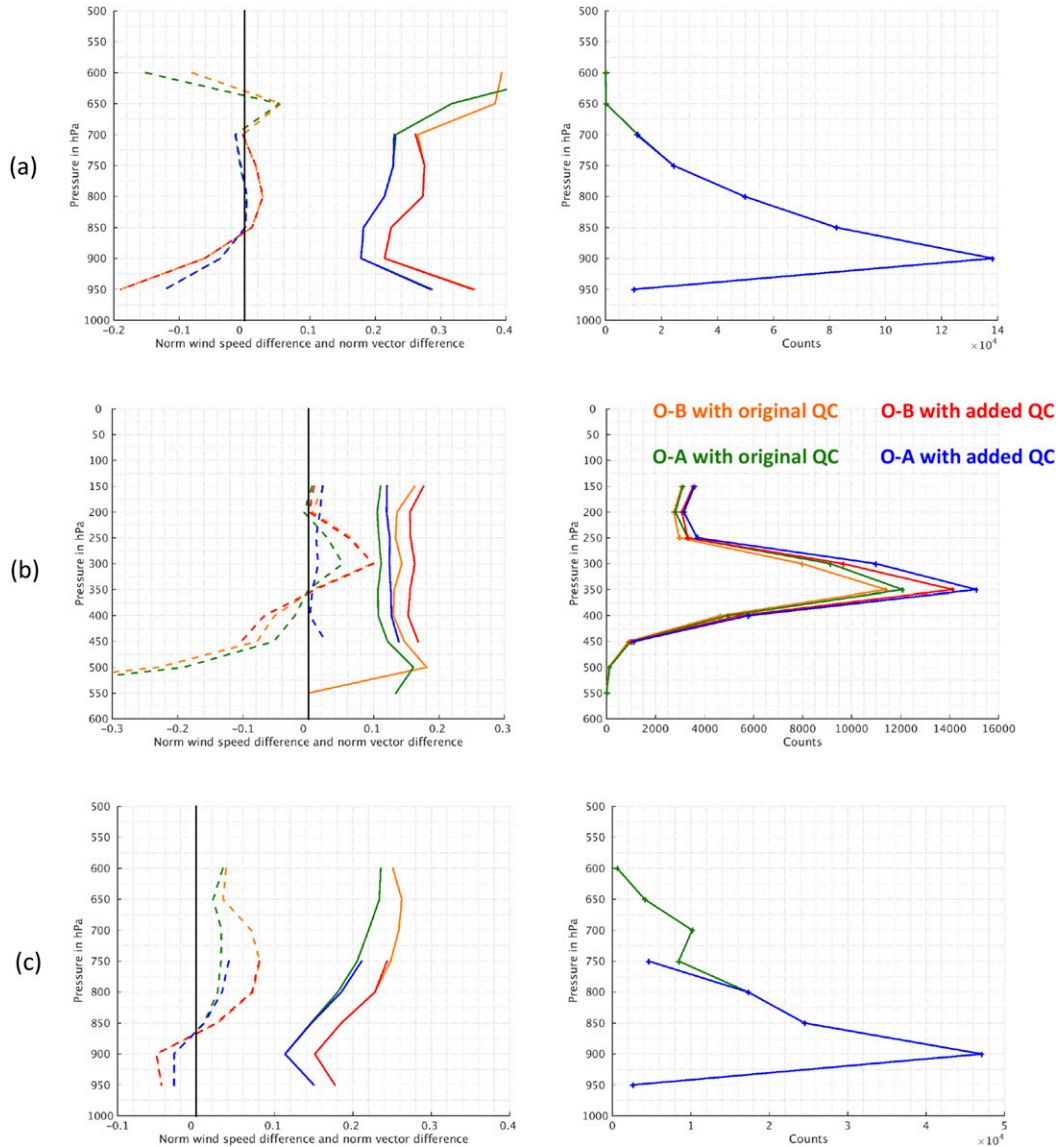
FIG. 4. Impact due to changes in QC procedures on (left) the mean AMV normalized speed departure from the background/analysis (dashed) and the standard deviation of the AMV normalized vector difference from the background/analysis (solid) binned at every 50 hPa and (right) the corresponding number of observations assimilated for the (a) SWIR-, (b) CAWV-, and (c) VIS-type AMVs for Hurricane Joaquin. Orange lines show the departure statistics and counts for the AMVs compared to the first-guess background state (O–B) while green lines show the count and statistics for the AMV departure with respect to the final analysis (O–A). Likewise, red (O–B) and blue (O–A) are the resulting count and statistics with the additional QC procedures. Statistics are calculated from the entire life cycle of Hurricane Joaquin.

were also checked using Tropical Storm Ida and Hurricane Kate and found to be consistent. Table 4 summarizes these QC procedures applied to the HWRF AMVs.

The observational errors for all five AMV types, as defined in the GDAS, are a function of pressure and are shown in Fig. 5. The observational errors range from $3.7 \, \mathrm{m \, s^{-1}}$ near the surface to $7 \, \mathrm{m \, s^{-1}}$ in the upper troposphere. The application of a gross error check for the AMVs is related to this error profile. SWIR-, CAWV-,

and VIS-type AMVs are rejected if their innovation exceeds 2.5 times the error obtained from the error profile. For reference, IR- and CTWV-type AMVs are rejected if their innovations exceed 1.3 times the error obtained from the error profile.

b. Examination of data impact on a single analysis

The ability to conduct an extensive analysis of the impact of the SWIR-, CAWV-, and VIS-type AMVs

TABLE 4. QC procedures applied to GOES hourly AMVs in GSI. QCs in boldface are additional checks.

QC to reject observations	AMV type subjected to this check
Pressure level of AMV < model tropopause − 50 hPa	SWIR, IR, CTWV, CAWV, and VIS
Pressure level of AMV > 950 hPa	SWIR, IR, CTWV, CAWV, and VIS
QI without forecast < 85	SWIR, IR, CTWV, and VIS
Normalized EE > 0.8 m s^{-1}	IR and CTWV
Pressure level of AMV > 800 hPa and normalized EE > 0.55 m s^{-1}	IR
Over land for latitude greater than 20°	IR
400 < pressure level of AMV < 800 hPa	IR
Pressure level of AMV > 400 hPa	CTWV
Wind direction > 50°	CAWV
Wind speed < 8 m s^{-1} and pressure level of AMV > 450 hPa	**CAWV**
Pressure level of AMV < 700 hPa	**SWIR**
Pressure level of AMV < 750 hPa	**VIS**

assimilation on tropical cyclone modeling is limited by the complexity of the HWRF setup as outlined in section 2b. Such an analysis is also not the focus of this study. However, examining a single analysis cycle provides information on the influence of the new AMV types on the analysis and demonstrates that the modified analysis increment is consistent with analysis increments without the new AMV types. In this section, two single cycles are examined: one from Hurricane Joaquin, a strong TC, and the other from Tropical Storm Ida, a weak TC. The geographical and vertical coverage patterns of the hourly AMV observations in assimilation domain 2 for both cycles are shown in Fig. 6. Observations accepted for assimilation are located mainly in the storm environment with the AMV data predominately in the lower and upper troposphere. The lack of AMVs near the TC center is due to the limits of the generation of AMVs by the data producer in cases of extreme changes in target direction and speed between images.

For Hurricane Joaquin, the 0000 UTC 2 October 2015 cycle was chosen. The HWRF had been cycling for 4 days. At this time, Joaquin had a minimum central pressure of 931 hPa and a maximum wind speed of 120 kt. Horizontal cross sections of analysis increment (analysis − first guess) of temperature and wind speed are taken at representative levels of the atmosphere and are plotted in Fig. 7 for CTRL and AMV1. Plotted in the third column are the differences of the analysis increments between CTRL and AMV1 to show where the analysis increments have changed from the assimilation of the new AMV types. In data assimilation, a correction is applied to the first guess based on a set of observations and estimated errors that are present in both the observations and the first guess. The spreading of information by the correlations within the background error covariance matrix resulted in analysis increments away from the observations. From the analysis increment plots of CTRL and AMV1, there is little change in the

wind speed analysis increments at 850 hPa. The analysis increment difference plot shows a slight strengthening of wind speed at the northeast quarter of the domain and a weakening of wind speed of up to 2 m s^{-1} in the southwestern corner of the domain. The change is influenced by both VIS- and SWIR-type AMVs (Fig. 6a) located in that region. At 250 hPa (Fig. 7b), the largest wind speed increment is located at 10°N, 75°W and is enhanced with the assimilation of the new AMV types. This region is dominated by the CAWV-type AMVs. Adjustments made to temperature from the winds are translated through the dynamical balances within the GSI. The temperature analysis increment plot indicates that with the assimilation of the SWIR-, CAWV-, and VIS-type AMVs, there is warming from the analysis adjustment near the center of the TC (Fig. 7c).

The meridional cross sections at 74.4°W of the first guess (contours) and analysis increment (shaded contours) of zonal wind velocity, temperature, and specific
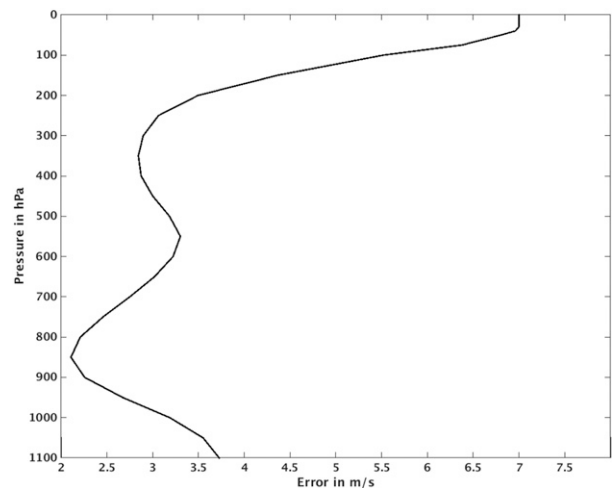

FIG. 5. Profile of observational error as a function of pressure used for SWIR-, CAWV-, and VIS-type AMVs.
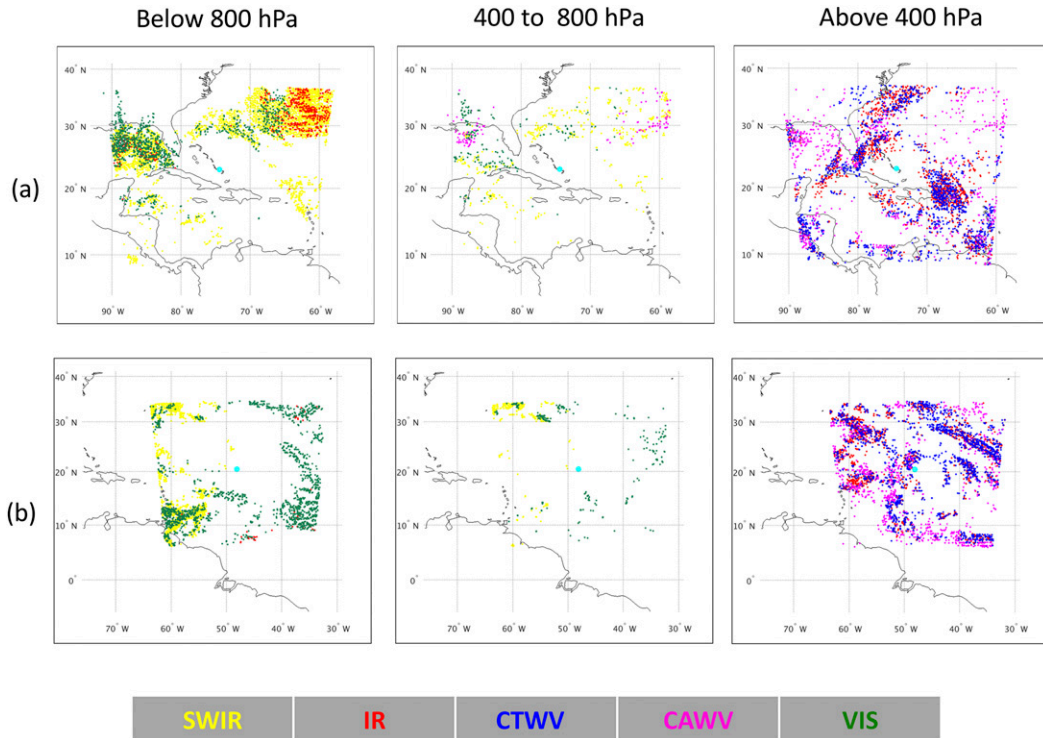
FIG. 6. Distribution of different AMV types assimilated in HWRF at three different layers of the atmosphere for one assimilation cycle for ghost domain d02. Storm center obtained from the NHC best track is marked with a cyan dot. (a) Hurricane Joaquin at 0000 UTC 2 Oct 2015 with the storm center located at 22.9°N, 74.4°W and (b) Tropical Storm Ida at 1200 UTC 21 Sep 2015 with the storm center located at 20.5°N, 48.1°W.

humidity for ghost domain 2 are shown in Fig. 8. Plotted in the third column of Fig. 8 are the differences in analysis increments to aid identification of change due to the addition of the new AMVs. In Fig. 8a, the reduction in zonal wind increment relative to the CTRL is most prominent in the midtroposphere south of the TC center, implying a weaker anticyclonic increment with the addition to the new AMV types. The u-component wind increment is also reduced above 200 hPa in the AMV1 experiment. Similar patterns are observed for ghost domain 3 (not shown). For temperature (Fig. 8b), the assimilation of the new AMV types causes less cooling near the TC center. Similarly, for specific humidity (Fig. 8c), there is less drying in the midtroposphere near the storm center when including the new AMV types. However, parts of the adjustment described are removed by the merging step prior to running forecast. In this step, for TC whose maximum wind speed is greater than 64 kt, the analysis increments from data assimilation are zeroed out within 150 km of the TC center and below 600 hPa. This area is indicated by the hashed region in each subplot in Fig. 8. Removing the analysis increments from GSI prevents the AMV wind-type observations and other observations within 150 km of the TC center from

influencing the inner core. Analysis increments are gradually introduced into the final analysis between 150 and 300 km.

Tropical Storm Ida had its lowest minimum central pressure of 1001 hPa and a maximum wind speed of 45 kt at 1200 UTC 21 September 2015. At this time, the HWRF had been cycling for 3 days. Plotted in Fig. 9 are analysis increments of temperature at 850 hPa, wind speed analysis increments at 850 and 250 hPa for CTRL and AMV1, and their differences. At 850 hPa, negative wind speed increments are found on the right side of the domain, and positive wind speed increments dominate the left side of the domain (Fig. 9a). These changes are caused by the VIS- and SWIR-type AMVs' presence in these regions, respectively (Fig. 6b). At 250 hPa (Fig. 9b), the CAWV-type AMVs enhanced the positive wind speed increments at 18°N, 35°W. Temperature increments are generally small (Fig. 9c). Meridional cross sections of the u-component wind at 48.1°W (Fig. 10a) show an increased anticyclonic increment at 350 hPa at 10°N. In Fig. 10b, cooling occurs at 20°N between 100 and 200 hPa and between 500 and 700 hPa. Above 400 hPa, the adjustment is due to the addition of the CAWV-type AMV. There is increased moisture
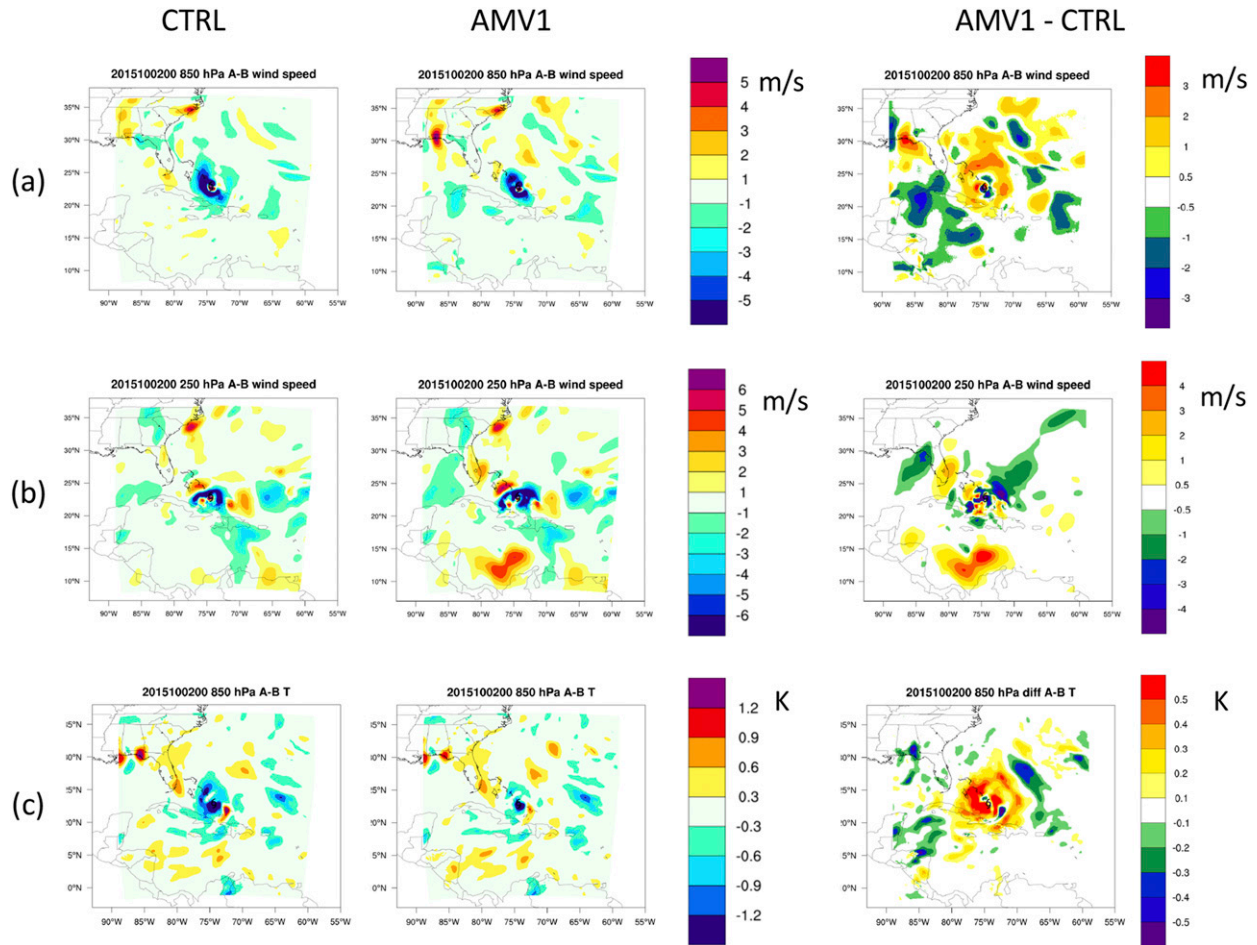
FIG. 7. Analysis increment and difference of ghost domain d02 for Hurricane Joaquin. (a) Wind speed (m s^{-1}) at 850 hPa, (b) wind speed (m s^{-1}) at 250 hPa, and (c) temperature (K) at 850 hPa at 0000 UTC 2 Oct 2015 for (left) CTRL, (center) AMV1, and (right) AMV1 − CTRL.

(Fig. 10c) at about 700 hPa, south of the storm center. From the distribution of AMVs assimilated between 400 and 800 hPa (Fig. 6b), few AMV observations are assimilated in this part of the troposphere. The adjustments observed are due to the spreading of information by the background error covariance matrix. As Ida's maximum wind speed is less than 64 kt, the full analysis increments are present in the final analysis. These increments will allow the impact obtained from the data assimilation to influence the TC inner core.

The magnitude of the correction made by the new AMVs on the first guess in both storms is incremental. Similar patterns in analysis increments are observed with and without the assimilation of the new wind types. Reviewing these two single cycles' analyses provides confidence that the addition of the new AMVs is consistent with the observations already present in the system.

4. Results

Atlantic tropical cyclones from the 2015 and 2016 hurricane seasons are used to assess the impact of adding hourly SWIR-, CAWV-, and VIS-type AMVs on tropical cyclone forecasts. The list of tropical cyclones used, the time period of each tropical cyclone when HWRF was run, and the total number of data assimilation cycles completed are shown in Table 5. This set includes a total of 25 tropical cyclones: five major hurricanes, five hurricanes, 13 tropical storms, and two tropical depressions. Tropical cyclone forecast skill is evaluated by comparing model forecasts against NHC's postprocessed best-track storm data.

The metrics used to measure the performance of tropical cyclone forecasts are track error in nautical miles (n mi; 1 n mi = 1.852 km), intensity error (kt), intensity bias (kt), and minimum central pressure error (hPa), as well as average 34-, 50-, and 64-kt wind radii
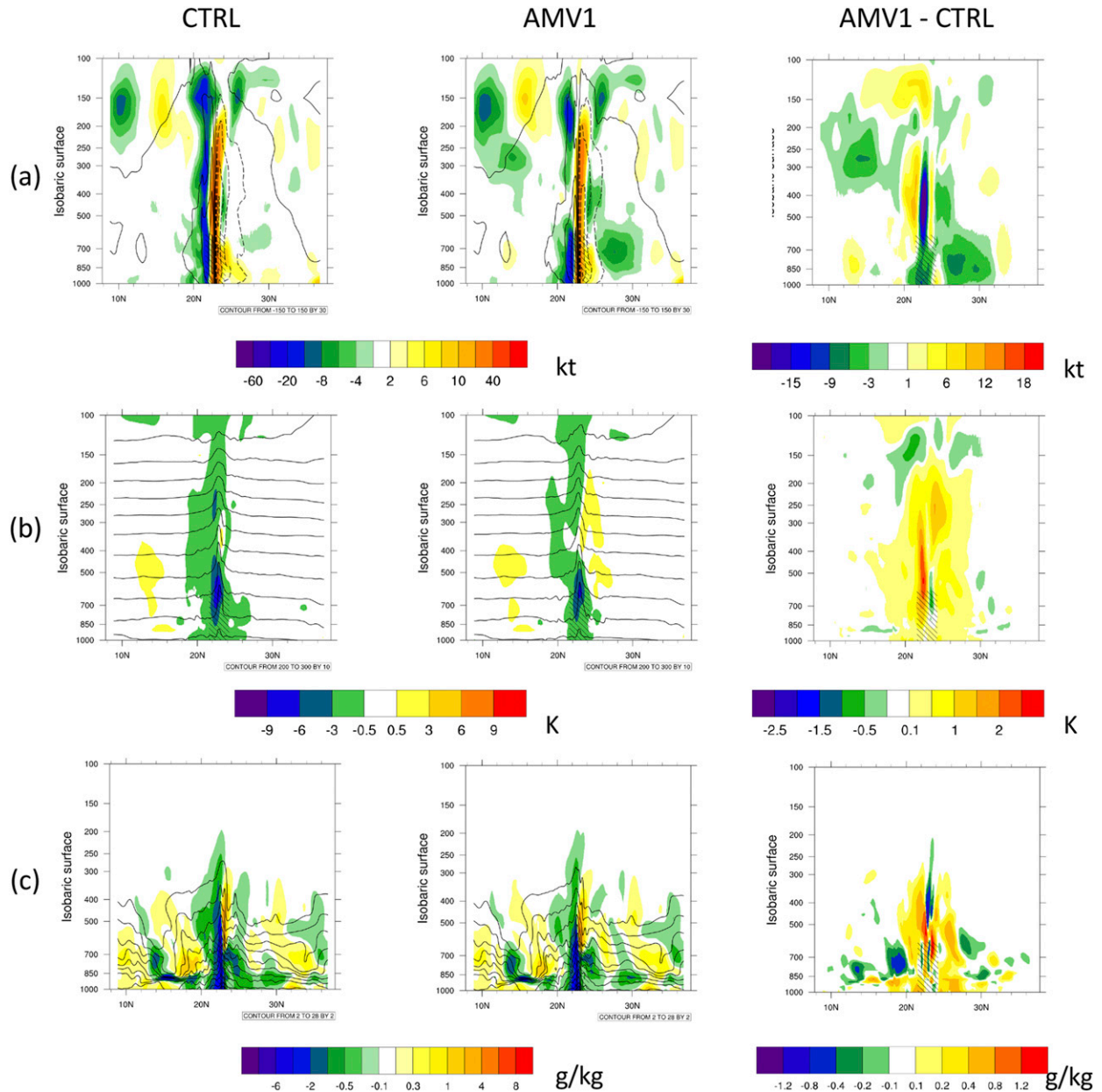
FIG. 8. First guess (black contours) and analysis increment (color shades) as well as differences for the meridional cross section of ghost domain d02 for Hurricane Joaquin. Shown are the (a) u-component wind (kt), (b) temperature (K), and (c) specific humidity (g kg^{-1}) at 0000 UTC 2 Oct 2015 for (left) CTRL, (center) AMV1, and (right) AMV1 − CTRL. The cross section was taken through the center of the storm defined by the NHC best track at 22.9°N, 74.4°W. The hashed region indicates area where analysis increments from GSI will be removed in the merging step.

errors. Track forecast error is defined as the great-circle distance between a cyclone's forecast position and the best-track position at the forecast verification time. The forecast track error is also decomposed into along-track and across-track errors. The along-track error indicates if the forecast is advancing the storm too fast or too slow. The across-track error is an indicator of the position of the storm, that is, if the forecast storm is to the right or to the left with respect to the observed track. Intensity error is defined as the absolute difference between the forecast intensity and the best-track intensity at verifying time. Intensity is defined as the maximum sustained 10-m winds. Mean wind radii errors at 34, 50, and 64 kt are the average of the wind radii errors at these speeds from all four quadrants of the TC. The radius is defined as the distance from the TC center to the location where
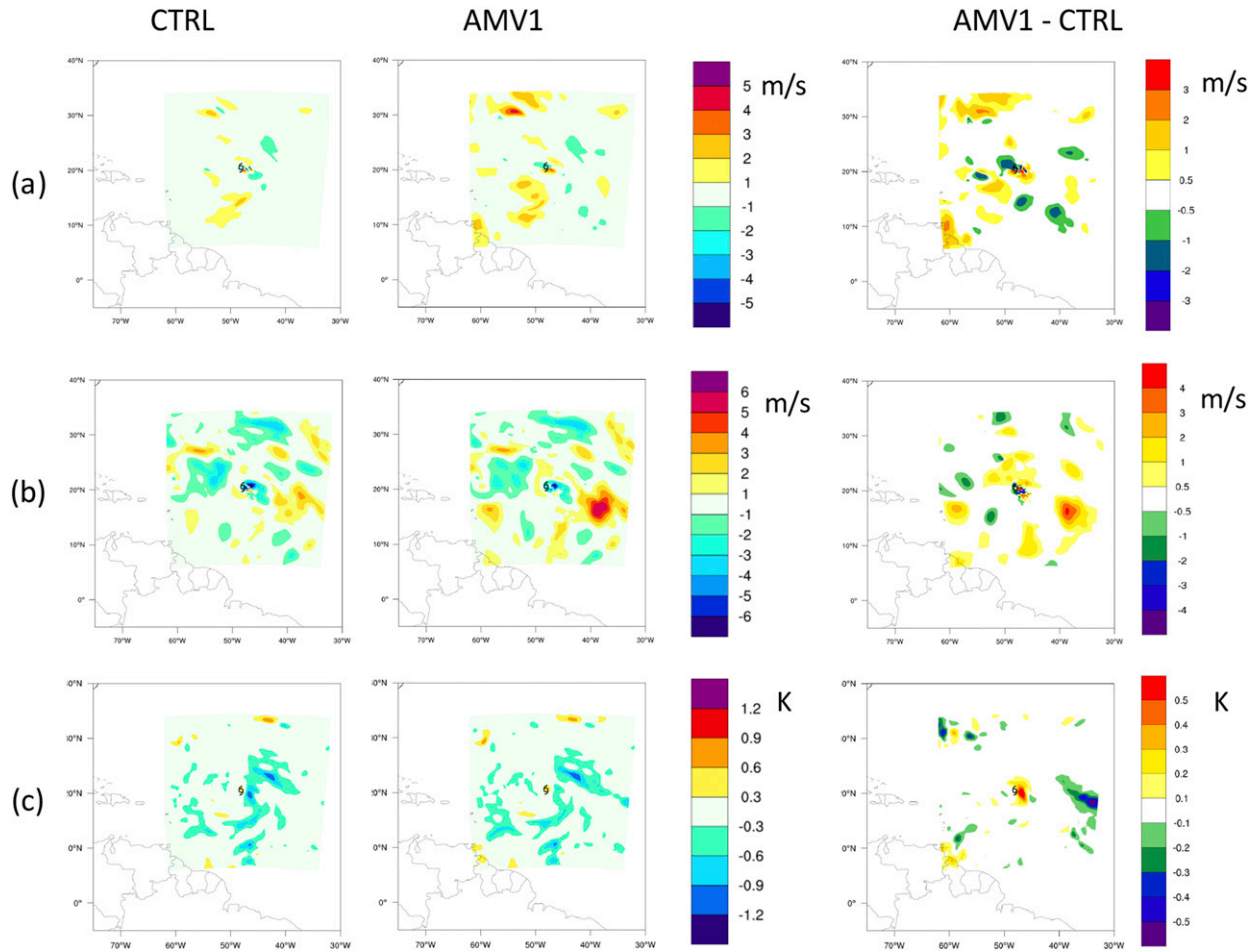
FIG. 9. Analysis increment and difference of ghost domain d02 for Tropical Storm Ida. (a) Wind speed (m s^{-1}) at 850 hPa, (b) wind speed (m s^{-1}) at 250 hPa, and (c) temperature (K) at 850 hPa at 1200 UTC 21 Sep 2015 for (left) CTRL, (center) AMV1, and (right) AMV1 − CTRL.

the tangential wind has the required speed magnitude. Mean wind radii can be used to measure the storm size between different experiments (Tallapragada et al. 2014). Two skill scores, the relative skill and the frequency of superior performance (FSP), are also used to access the performance of the assimilation of the new wind types against other models. The relative skill is used as a measure of the magnitude of improvement/degradation between the forecasts from the assimilation runs and the climatology and persistence (CLIPER) and Statistical Hurricane Intensity Forecast (SHIFOR) statistical models. This metric is further normalized with the CTRL run for convenience in this manuscript. The FSP measures the frequency of model producing a better forecast than another model (Velden and Goldenberg 1987). The FSP looks at forecasts from different models present in the NOAA Automated Tropical Cyclone Forecast (ATCF) guidance comma-delimited files (A-deck) and ranks the control and

experiment relative to these models. A value larger than 50% is indicative that the control/experiment forecast on average performs better than the other models more than half the time. This skill score does not include the effects of outliers and thus with a sufficiently large sample can show the overall consistency of the model performance. Both skill scores can be evaluated together to better assess model performance. For example, if FSP > 50 but the skill is negative, this implies that on average there is forecast improvement, but there are some strong outliers.

a. All storms statistics

Statistics are first computed using all Atlantic tropical cyclones from both the 2015 and 2016 hurricane seasons. For figures described in this section and the next, red lines indicate CTRL and blue lines indicate AMV1. The number of samples used in deriving the statistics for each forecast hour is labeled in green along
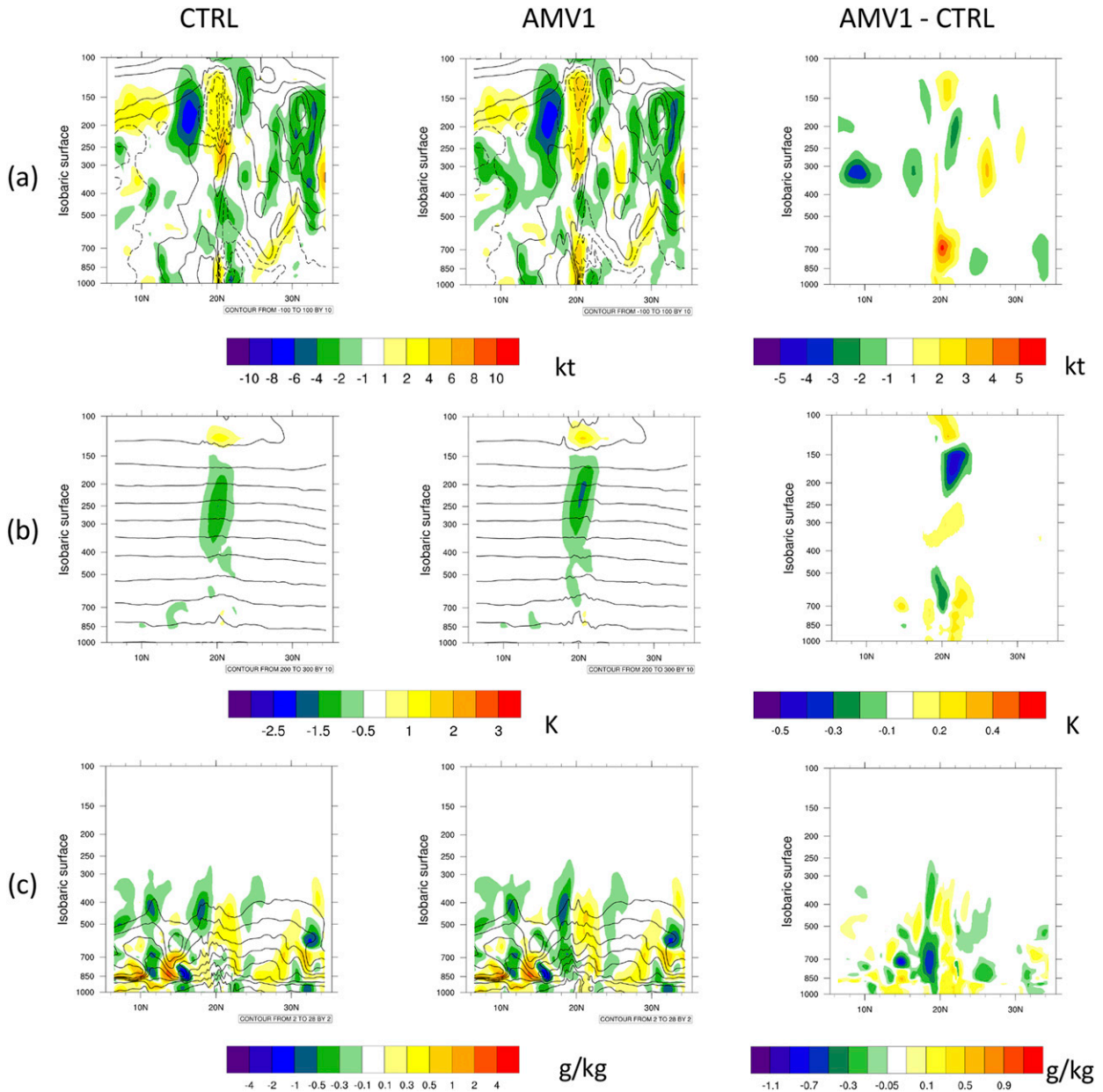
FIG. 10. First guess (black contours) and analysis increment (shaded contours) as well as difference for the meridional cross section of ghost domain d02 for Tropical Storm Ida. The (a) u-component wind (kt), (b) temperature (K), and (c) specific humidity (g kg^{-1}) at 1200 UTC 21 Sep 2015 for (left) CTRL, (center) AMV1, and (right) AMV1 − CTRL. The cross section was taken through the center of the storm defined by the NHC best track at 20.5°N, 48.1°W.

the secondary axis. The error bars represent a 95% statistical confidence interval.

Forecasts of tropical cyclone intensity are improved when the new AMV types were added for 36-h forecasts and beyond (Fig. 11a). The largest reduction of intensity error occurs between the 72- and 96-h forecasts when comparing AMV1 to the CTRL. The improvement is, however, not statistically significant at the 95% confidence level. Intensity bias (Fig. 11b)

shows that the CTRL has a less negative intensity bias when the assimilation of the AMV wind types reduced the intensity error. The minimum central pressure error shows improvements for AMV1 compared to CTRL beyond the 30-h forecasts (Fig. 11c). The minimum center pressure bias is also reduced for AMV1 (not shown) beyond the 36-h forecasts.

The 34- and 50-kt wind radii forecasts (Figs. 12a,b) show improvement up to the 78- and 108-h forecasts,

TABLE 5. List of TCs used in this study. Storm categorization is extracted from NHC reports.

Start and end date	Tropical cyclone name	Storm category	No. of assimilation cycles
1800 UTC 13 Jul–0000 UTC 15 Jul 2015	Claudette	Tropical storm	6
1200 UTC 18 Aug–1200 UTC 24 Aug 2015	Danny	Major hurricane	25
0000 UTC 25 Aug–1200 UTC 29 Aug 2015	Erika	Tropical storm	19
0600 UTC 30 Aug–1800 UTC 6 Sep 2015	Fred	Hurricane	31
1200 UTC 5 Sep–1200 UTC 9 Sep 2015	Grace	Tropical storm	17
0600 UTC 9 Sep–1800 UTC 11 Sep 2015	Henri	Tropical storm	15
1200 UTC 16 Sep–0000 UTC 20 Sep 2015	Nine	Tropical depression	15
1200 UTC 18 Sep–1800 UTC 27 Sep 2015	Ida	Tropical storm	38
0000 UTC 28 Sep–1200 UTC 7 Oct 2015	Joaquin	Major hurricane	39
0000 UTC 9 Nov–0600 UTC 12 Nov 2015	Kate	Hurricane	14
1200 UTC 27 May–0000 UTC 5 Jun 2016	Bonnie	Tropical storm	35
1200 UTC 5 Jun–1800 UTC 7 Jun 2016	Colin	Tropical storm	10
0000 UTC 20 Jun–0600 UTC 21 Jun 2016	Danielle	Tropical storm	6
1200 UTC 2 Aug–1200 UTC 6 Aug 2016	Earl	Hurricane	16
0000 UTC 17 Aug–1200 UTC 23 Aug 2016	Fiona	Tropical storm	27
1800 UTC 22 Aug–0600 UTC 3 Sep 2016	Gaston	Major hurricane	45
1200 UTC 28 Aug–1800 UTC 31 Aug 2016	Eight	Tropical depression	18
1800 UTC 28 Aug–1200 UTC 6 Sep 2016	Hermine	Hurricane	33
1200 UTC 12 Sep–1200 UTC 16 Sep 2016	Ian	Tropical storm	16
0000 UTC 14 Sep–0600 UTC 19 Sep 2016	Julia	Tropical storm	22
1200 UTC 14 Sep–1200 UTC 25 Sep 2016	Karl	Tropical storm	44
1800 UTC 19 Sep–0000 UTC 25 Sep 2016	Lisa	Tropical storm	22
1200 UTC 28 Sep–1800 UTC 9 Oct 2016	Mathew	Major hurricane	46
1200 UTC 4 Oct–0600 UTC 18 Oct 2016	Nicole	Major hurricane	56
0600 UTC 21 Nov–0000 UTC 25 Nov 2016	Otto	Hurricane	16

respectively. With the assimilation of the new AMV types, the 64-kt wind radius errors (Fig. 12c) are smaller than the CTRL for 36-h forecasts and beyond. The improvements in storm sizes are not statistically significant at the 95% confidence level.

Figure 13 shows the track error performance with and without the addition of the new AMV types. Inclusion of the SWIR-, CAWV-, and VIS-type AMVs has a neutral impact on the total track forecast error for up to the 72-h forecasts with slightly worse performance beyond that point (Fig. 13a). A possible reason for the neutral impact on the total track error is that these three AMV types are not assimilated in NOAA's operational GDAS/GFS. The GDAS and GFS analyses provide the initial and boundary conditions for the HWRF. The large-scale environmental flow plays a major role in tropical storm tracks (Cangialosi and Franklin 2017). The inconsistencies in the large-scale environmental flow between the initial and boundary conditions and the HDAS analyses contribute to a lack of improvements in the HWRF track forecasts. To better understand the total track performance, the total track error is decomposed into along-track and across-track forecast errors (Figs. 13b,c). These two track metrics show that the assimilation of the new AMV types improve the storm advancement (along track) forecasts and the veering of the forecast path

(across track) from the observed track out to the 72-h forecasts.

The range in the track-relative skill is between −4% and 2%. A positive relative skill of less than 5% is obtained for 3–9- and 15–33-h forecasts for track. Track-relative skill for AMV1 is negative beyond 36-h forecasts. Total track error FSP performs better for the experiment for the 6-h forecasts. Beyond that, track FSP for the control simulation performs slightly better. Track error FSP and relative skill are consistent from 3- to 9-h forecasts. Figures for the total track error relative skill and FSP are not shown. Figure 14a shows positive relative skill for intensity beyond the 36-h forecasts. This positive relative skill reaches its maximum of 15% between 84- and 108-h forecasts. FSP for intensity error (Fig. 14b) is greater than 50% between 36- and 96-h forecasts and consistent with relative skill.

b. Strong and weak storm vortices

Model tropical cyclone vortices are binned based on their intensity at the initial forecast time and statistics of their forecast performance with and without the assimilation of SWIR-, CAWV-, and VIS-type AMVs are computed. Since vortex initialization is performed at the beginning of each assimilation cycle, the initial model storm intensity is very close to that of the NHC best
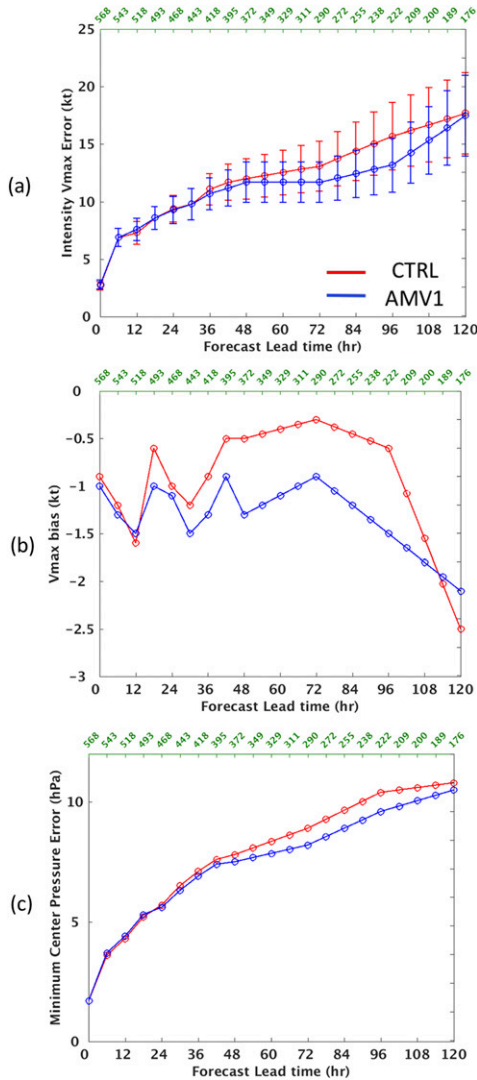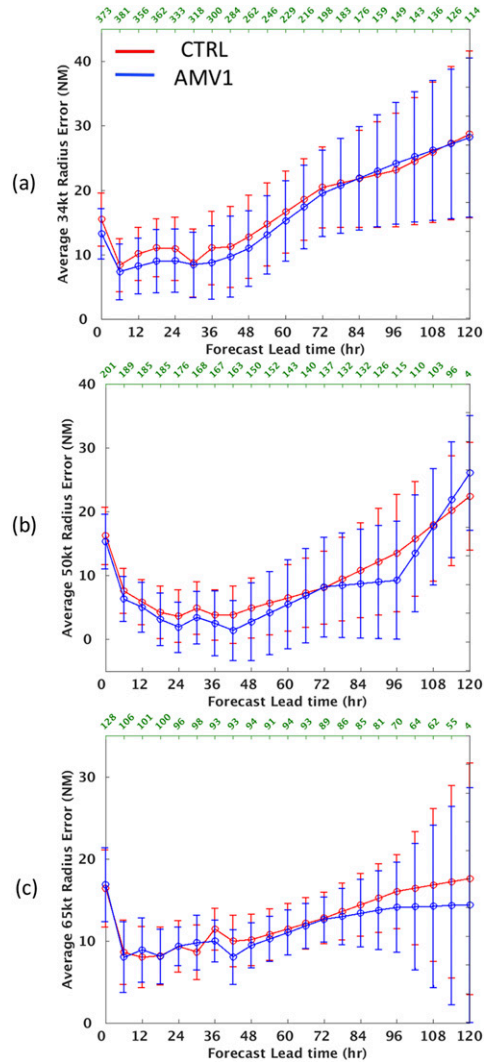
FIG. 11. Verification statistics for the 2015 and 2016 hurricane seasons for control (red) and experiment with the addition of SWIR-, CAWV-, and VIS-type AMVs (blue). Shown are the (a) intensity error measured using maximum sustained 10-m winds, (b) intensity bias, and (c) minimum central pressure. Error bars represent a 95% confidence interval. The number of samples used in deriving these statistics is shown in green.

FIG. 12. Verification statistics for the 2015 and 2016 hurricane seasons for control (red) and experiment with the addition of SWIR-, CAWV-, and VIS-type AMVs (blue). The average (a) 34-, (b) 50-, and (c) 64-kt radius errors. Error bars represent a 95% confidence interval. The number of samples used in deriving these statistics is shown in green.

track. If the model initial intensity is greater than 64 kt, then the storm vortex is classified as strong; otherwise, it is classified as weak. The choice of the 64-kt thresholds follows the Saffir–Simpson hurricane wind scale (http://www.nhc.noaa.gov/pdf/sshws.pdf) for hurricane classification.

Figure 15 shows plots of the intensity error, the minimum central pressure error, and the minimum central pressure bias for strong and weak TC vortices as a function of forecast lead time. Assimilation of the new AMVs shows a positive impact for storm intensity for both

groups of TC vortices (Fig. 15a). Comparing AMV1 to CTRL, the positive impact in intensity error reduction is apparent after the 24- and 36-h forecasts for the strong and weak TC storm vortices. For both groups of storm vortices, a positive impact is observed out to the 126-h forecasts. The magnitude of the intensity error reduction is larger for weak TC vortices at longer lead hours compared to strong TCs. In both cases, the intensity error reduction is statistically not significant at the 95% confidence interval. Improvement in the intensity error in weak TC vortices is associated with a reduction in the positive intensity bias (Fig. 15b). Error reduction in
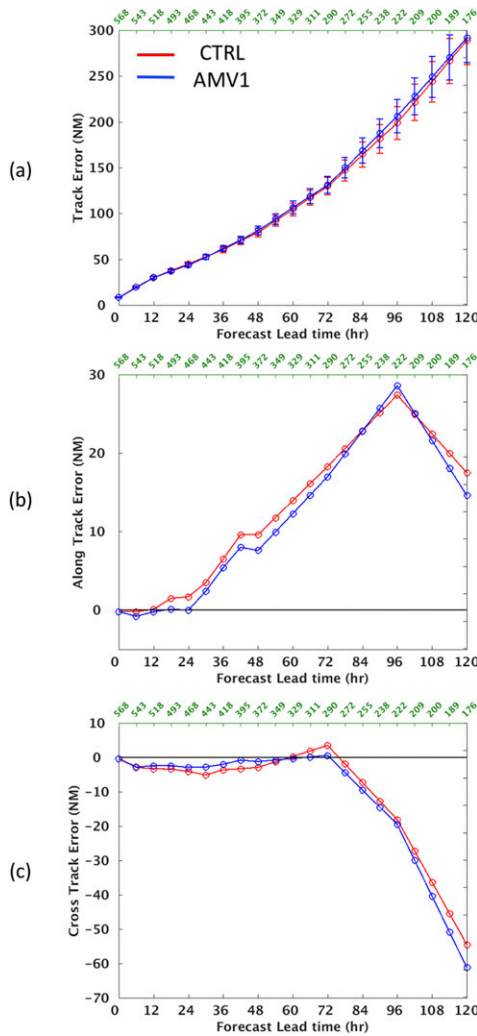
FIG. 13. Verification statistics for the 2015 and 2016 hurricane seasons for control (red) and experiment with the addition of SWIR-, CAWV-, and VIS-type AMVs (blue). Shown are the (a) track error, (b) along-track error, and (c) across-track error. Error bars represent a 95% confidence interval. The number of samples used in deriving these statistics is shown in green.
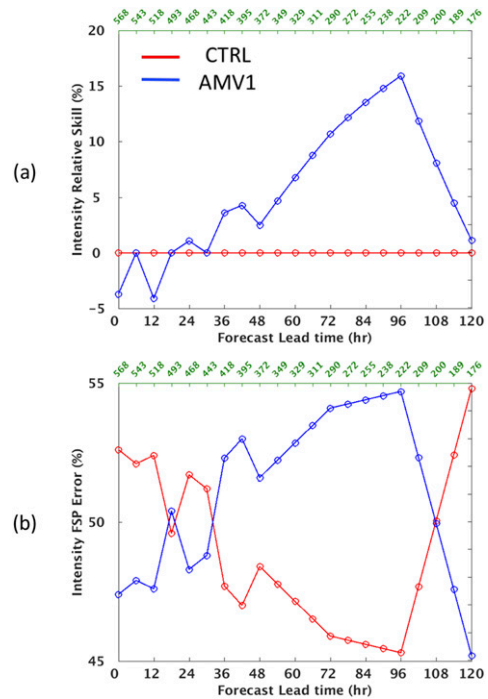

FIG. 14. Skill performance for the 2015 and 2016 hurricane seasons for control (red) and experiment with the addition of SWIR-, CAWV-, and VIS-type AMVs (blue). Shown are the (a) intensity relative skill and (b) intensity error FSP. The number of samples used in deriving these statistics is shown in green.

minimum center pressure error for weak TC vortices is observed for lead times greater than 48-h forecasts (Fig. 15c) with the assimilation of the new AMV types. The impact on strong TC vortices is mixed. Reduction in minimum central pressure bias (not shown) is in line with the reduction of the minimum central pressure error. For weak storm vortices, the minimum central pressure bias error is smaller for AMV1 compared to CTRL beyond the 78-h forecasts. For strong storm vortices, a reduction in minimum central pressure bias occurs in forecasts up to 60 h. For intensity relative skill (Fig. 15d), positive skill is obtained for both strong and weak TC vortices beyond the 48-h forecasts for AMV1. The addition of the three new AMV types produces

better forecasts, resulting in improved intensity forecasts compared to those of the CTRL between the 36- and 96-h forecasts for weak storm vortices. For strong TC vortices, AMV1 produces superior storm intensity predictions beyond the 66-h forecasts (Fig. 15e).

Regardless of the strength of the TC vortex determined at the initial forecast time, assimilation of the new AMVs has a neutral impact on the total track error (Fig. 16a) up to the 48-h forecasts. Improvement in track error is observed beyond 60-h forecasts for strong TC vortices. For weak TC vortices, degradation in track error forecasts is observed beyond 48-h forecasts. The total track error is again decomposed into along-track and across-track errors to identify any positive impact from adding the new AMV types. Comparing AMV1 with CTRL, along-track error improvement is observed for weak TC vortices after 36-h forecasts. (Fig. 16b). The influence of the new AMV types on along-track errors is negative for strong tropical cyclone vortices. In the case of across-track error, both strong and weak TC vortices achieve positive impacts out to the 90-h forecasts (Fig. 16c) with the assimilation of hourly SWIR-, CAWV-, and VIS-type AMVs. For track-relative skill performance, Fig. 16d shows that the assimilation of the three AMV types has a negative influence on weak TC
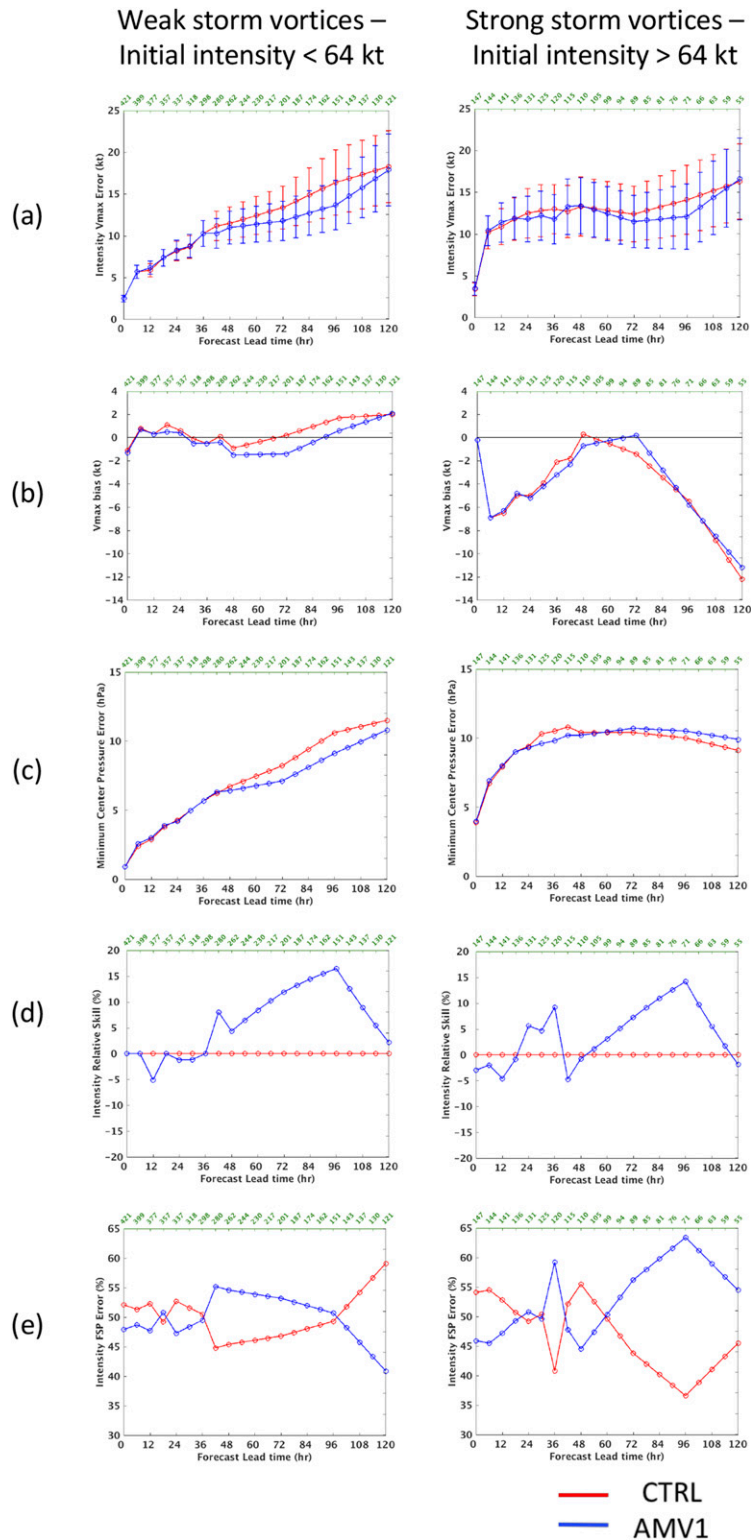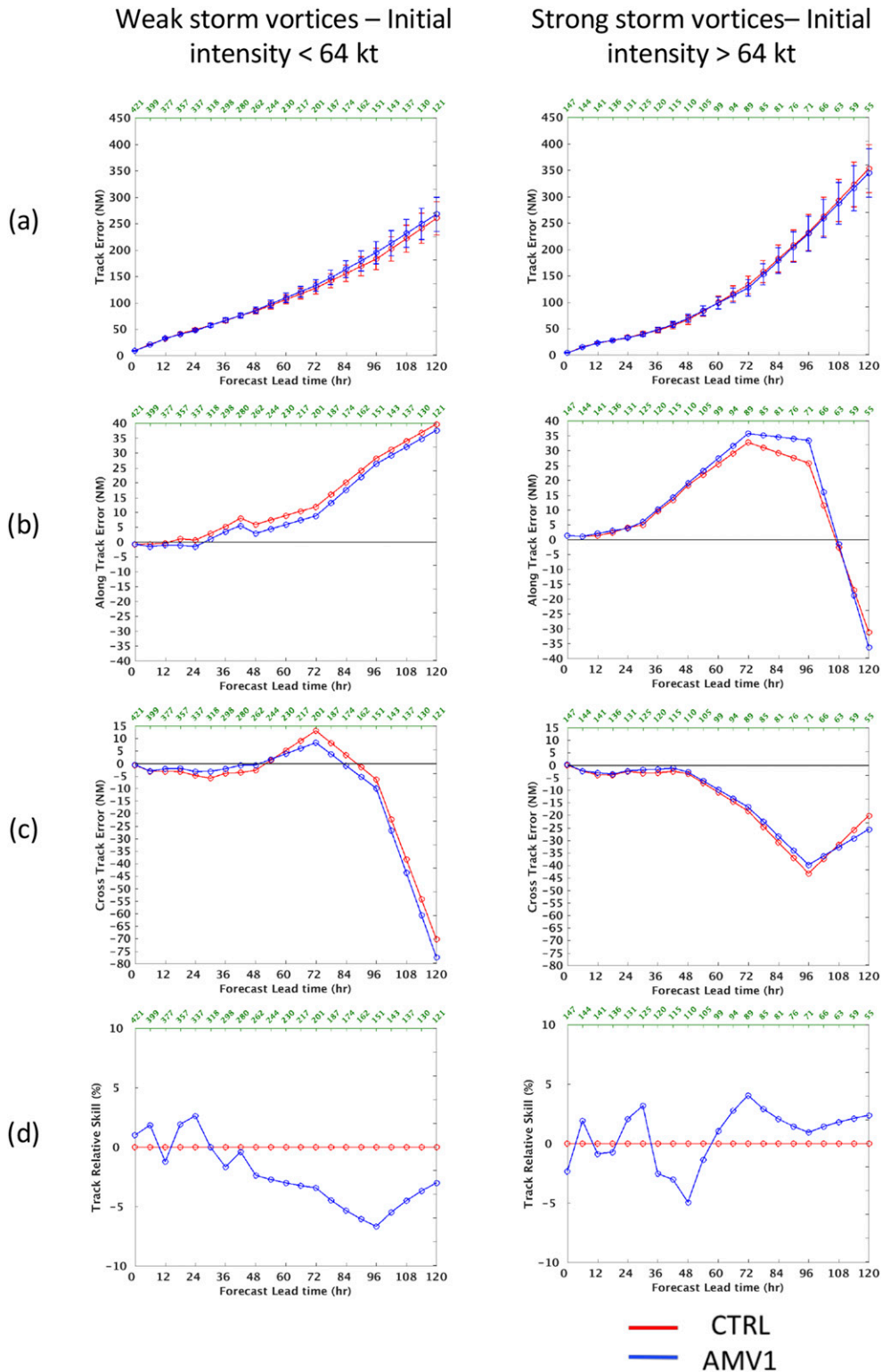
FIG. 15. Verification statistics for weak and strong storm vortices grouped based on initial model intensity at each cycle. Control is shown in red and the experiment with the addition of SWIR-, CAWV-, and VIS-type AMVs in blue. Shown are the (a) intensity error, (b) intensity bias, (c) minimum central pressure, (d) intensity relative skill, and (e) intensity FSP error. Error bars represent a 95% confidence interval. The number of samples used in deriving these statistics is shown in green.
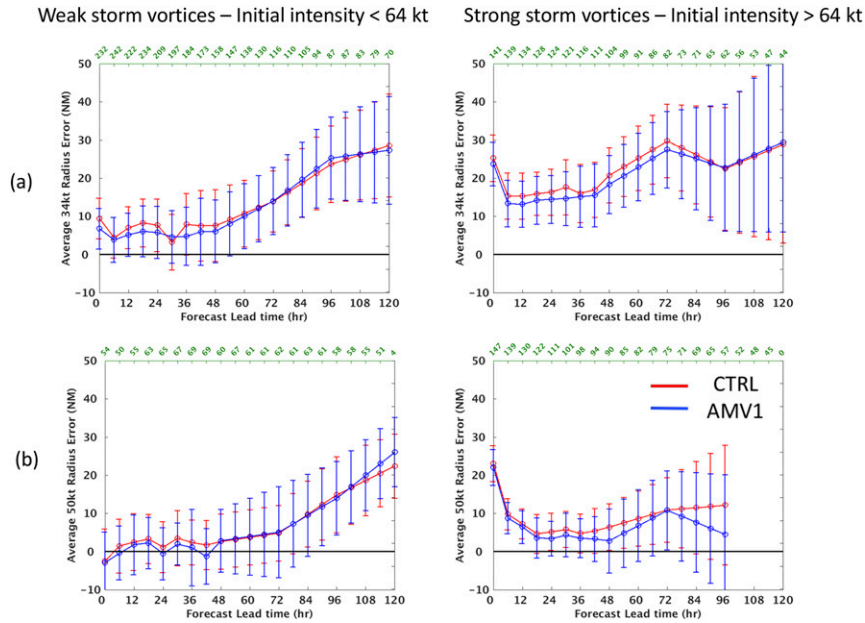
FIG. 16. Verification statistics for weak and strong storm vortices grouped based on initial model intensity at each cycle. Control is shown in red and the experiment with the addition of SWIR-, CAWV-, and VIS-type AMRs in blue. Shown are the (a) total track error, (b) along-track error, (c) across-track error, and (d) track relative skill error. Error bars represent a 95% confidence interval. The number of samples used in deriving these statistics is shown in green.

Weak storm vortices – Initial intensity < 64 kt   Strong storm vortices – Initial intensity > 64 kt

FIG. 17. Verification statistics for strong and weak storm vortices grouped based on model initial intensity at each cycle. Control is shown in red and the experiment with the addition of SWIR-, CAWV-, and VIS-type AMVs in blue. Shown are the (a) 34- and (b) 50-kt wind radii. Error bars represent a 95% confidence interval. The number of samples used in deriving these statistics is shown in green.

vortices' total track error for most of the forecast time periods. In the case of the strong TC vortices, the result is mixed out to the 60-h forecasts but becomes positive beyond that time. Examining the track error FSP shows that the experiments with the assimilation of SWIR-, CAWV-, and VIS-type AMVs (i.e., AMV1) do not produce sufficient superior forecasts compared to the CTRL experiment for weak storm vortex track errors. The results are mixed for strong TC vortices for forecasts less than 60 h (not shown).

Figure 17 shows storm radii forecast performance for both categories of TC vortices. Positive impact for more forecast lengths is achieved for both the 34- and 50-kt wind radii for strong TC vortices with the addition of the three new AMV types. For the 34-kt wind radius, error is reduced out to the 72-h forecasts for the weak TC vortices and 96-h forecasts for the strong TC vortices. The 50-kt wind radius error is reduced out to 48- and 96-h forecasts for weak and strong TC vortices, respectively. The improvement is statistically not significant at the 95% confidence level. The impact on the 64-kt wind radii is neutral (not shown).

Statistics show that the assimilation of the new AMV types has a positive impact for both types of TC vortices, but with metrics for weak TC vortices seeing greater error reduction. This is consistent with the findings in

Tong et al. (2018). Tong et al. found that assimilating high-density observations in the TC inner core produces better intensity forecasts for tropical storms as data assimilation corrects the large positive intensity bias introduced by vortex initialization for weak storms. In the case of strong TCs, the merging step in HWRF removes the data assimilation impact within 150 km of the TC center, inhibiting data assimilation from correcting the intensity bias.

5. Summary

In this study, hourly SWIR-, CAWV-, and VIS-type AMVs are added to the hourly IR- and CTWV-type AMVs for assimilation using the 2016 operational HWRF Model. New QC procedures were added to GSI to tighten the selection criteria of the new AMV types, while the existing quality control procedures were reviewed and customized for the assimilation of AMVs in HWRF. The changes made are as follows. 1) The minimum threshold wind speed of CAWV-type AMVs was lowered from 10 to 8 m s^{-1} to increase the number of CAWV-type AMVs for assimilation. 2) Low-level AMVs were limited in the vertical extent by rejecting AMVs with pressure values less than a set level; for SWIR-type AMVs, this value is 700 hPa and for VIS-type AMVs the cutoff is at 750 hPa. Likewise, upper-level CAWV-type

AMVs are not used if their pressure values are greater than 450 hPa. 3) Observational errors for the new AMV types are set to range from $3.7\,\mathrm{m\,s^{-1}}$ near the surface to $7\,\mathrm{m\,s^{-1}}$ at the middle of the troposphere and above.

Twenty-five Atlantic tropical cyclones from both the 2015 and 2016 hurricane seasons examined in this study provided statistics used to assess the impact from the assimilation of the hourly SWIR-, CAWV-, and VIS-type AMVs. There are five major hurricanes, five hurricanes, 13 tropical storms, and two tropical depressions in this set of storms. Metrics used to measure changes in tropical cyclone forecast skill include track error, intensity error, minimum central pressure error, and wind radii (storm size). Forecasts generated from experiments assimilating the three new hourly AMV types are compared with forecasts from the control HWRF analysis using an operational configuration.

Results from the assimilation of hourly SWIR-, CAWV-, and VIS-type AMVs show improvements in intensity forecasts. The magnitude of improvement of intensity forecasts is larger at longer lead times. A reduction in minimum central pressure errors from 30-h forecasts onward is also obtained when the SWIR-, CAWV-, and VIS-type AMVs are added. In terms of storm size, which is measured using the average 34- and 50-kt wind radii, improvement is achieved for the first 78- and 108-h forecasts, respectively, when new AMV types are used. In terms of intensity skill score, assimilation of the SWIR-, CAWV-, and VIS-type AMVs improves the intensity after 36 forecasts hours. The magnitude of improvement is as large as 15% between the 84- and 108-h forecasts. Analyses from AMV1 also produce a higher frequency of forecasts superior to the CTRL between the 36- and 96-h forecasts. Although the overall impact on track error forecasting is neutral, analyzing the along-track and across-track errors reveals that the translational speed of storms and the deflection of forecast paths compared to the observed path have improved out to 72-h forecasts.

TC vortices are binned based on their model intensity at the initial forecast time. Statistics related to forecast performance are calculated with and without the assimilation of the new AMV wind types. Results reveal that the assimilation of SWIR-, CAWV-, and VIS-type AMVs show positive impacts on different metrics for both groups of vortices. Intensity error improvement begins after 24-h forecasts for the strong storms, and the positive impact starts after 36-h forecasts for the weak storms. The magnitude of the intensity error reduction is larger for weak storms at longer forecast lead hours. The minimum central pressure error of weak storms also improved beyond the 48-h forecasts. Reduction in minimum central pressure bias occurs up to the 60-h
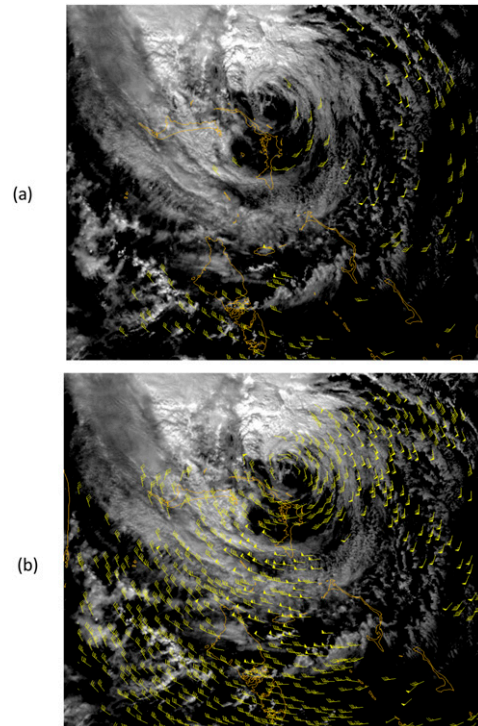

Fig. 18. Low-level (700–950 hPa) wind vectors using visible images for Hurricane Sandy. (a) Current operational AMVs derived from 15-min images via the heritage winds algorithm. (b) AMVs derived from 5-min images using the GOES-R nested tracking winds algorithm.

forecasts for the strong storm vortices and after 78-h forecasts for the weak storm vortices. The intensity relative skill performance shows that positive influence begins at a later time for strong storm vortices compare to the weak ones. Strong storm vortices have smaller storm size errors over longer forecast periods compared to the weak storm vortices. Small improvements in track forecast are observed for strong storm vortices at longer lead times. Results indicated that the impact of the assimilation of the new AMV wind types is dependent on the initial intensity of the TC vortex.

In summary, this research found that the tropical cyclone intensity forecast benefits most from the assimilation of more hourly AMVs. Other metrics such as minimum central pressure error and wind radii error indicate better forecasts have been produced from analyses that include the assimilation of the three new AMV types. Given the positive results obtained from this study, these new types of AMVs have been accepted into the operational HWRF assimilation system beginning with the 2017 hurricane season even though the results are statistically insignificant at the 95% confidence level.

The next step is to assimilate AMVs derived from the *GOES-16* Advanced Baseline Imager (ABI), which

replaced GOES-East in January 2018. These AMVs, derived using a new nested-tracking algorithm (Bresky et al. 2012), have better quality and are at higher spatial and temporal resolution (Fig. 18). According to Bresky et al. (2012), AMVs derived from the new nested tracking algorithm have reduced the low speed bias and the improved root-mean-square-error. A study conducted by Velden et al. (2017), assimilating *GOES-13* AMVs derived using this new algorithm on three Atlantic tropical cyclones shows a modest positive impact on HWRF forecasts. These AMVs will also be assimilated in NCEP's GDAS, providing better and more consistent initial conditions for HWRF. A data assimilation system that allows for the simultaneous assimilation of asynchronous observations such as the 4DEnVar developed within the HWRF framework (Lu et al. 2017) can further utilize the temporal information of the *GOES-16* AMVs.

REFERENCES

Aberson, S. D., 2011: The impact of dropwindsonde data from the THORPEX Pacific Area Regional Campaign and the NOAA hurricane field program on tropical cyclone forecasts in the Global Forecast System. *Mon. Wea. Rev.*, **139**, 2689–2703, https://doi.org/10.1175/2011MWR3634.1.

——, and J. L. Franklin, 1999: Impact on hurricane track and intensity forecasts of GPS dropwindsonde observations from the first-season flights of the NOAA Gulfstream-IV jet aircraft. *Bull. Amer. Meteor. Soc.*, **80**, 421–427, https://doi.org/10.1175/1520-0477(1999)080<0421:IOHTAI>2.0.CO;2.

Arakawa, A., and W. H. Schubert, 1974: Interaction of a cumulus cloud ensemble with the large-scale environment, part I. *J. Atmos. Sci.*, **31**, 674–701, https://doi.org/10.1175/1520-0469(1974)031<0674:IOACCE>2.0.CO;2.

Bayler, G., and H. Lewit, 1992: The Navy Operational Global and Regional Atmospheric Prediction System at the Fleet Numerical Oceanography Center. *Wea. Forecasting*, **7**, 273–279, https://doi.org/10.1175/1520-0434(1992)007<0273:TNOGAR>2.0.CO;2.

Berger, H., R. Langland, C. S. Velden, C. A. Reynolds, and P. M. Pauley, 2011: Impact of enhanced satellite-derived atmospheric motion vector observations on numerical tropical cyclone track forecasts in the western North Pacific during TPARC/TCS-08. *J. Appl. Meteor. Climatol.*, **50**, 2309–2318, https://doi.org/10.1175/JAMC-D-11-019.1.

Biswas, M. K., L. Carson, K. Newman, L. Bernardet, and C. Holt, 2016a: Community HWRF users' guide V3.8a. NCAR Developmental Testbed Center Rep., 149 pp., http://www.dtcenter.org/HurrWRF/users/docs/users_guide/HWRF_v3.8a_UG.pdf.

——, and Coauthors, 2016b: Hurricane Weather Research Forecasting (HWRF) Model: 2016 scientific documentation.

NCAR Developmental Testbed Center Rep., 95 pp., http://www.dtcenter.org/HurrWRF/users/docs/scientific_documents/HWRFv3.8a_ScientificDoc.pdf.

Bormann, N., K. Salonen, C. Peubey, T. McNally, and C. Lupu, 2012: An overview of the status of the operational assimilation of AMVs at ECMWF. *Proc. 11th Int. Winds Workshop*, Auckland, New Zealand, EUMETSAT, https://www.eumetsat.int/website/home/News/ConferencesandEvents/DAT_2039311.html.

Bresky, W., J. Daniels, A. Bailey, and S. Wanzong, 2012: New methods towards minimizing the slow speed bias associated with atmospheric motion vectors (AMVs). *J. Appl. Meteor. Climatol.*, **51**, 2137–2151, https://doi.org/10.1175/JAMC-D-11-0234.1.

Cangialosi, J. P., and J. L. Franklin, 2017: 2016 hurricane season. National Hurricane Center Forecast Verification Rep., 72 pp., https://www.nhc.noaa.gov/verification/pdfs/Verification_2016.pdf.

Chen, F., and J. Dudhia, 2001: Coupling an advanced land surface–hydrology model with the Penn State–NCAR MM5 modeling system. Part I: Model description and implementation. *Mon. Wea. Rev.*, **129**, 569–585, https://doi.org/10.1175/1520-0493(2001)129<0569:CAALSH>2.0.CO;2.

Chou, K.-H., C.-C. Wu, P.-H. Lin, S. D. Aberson, M. Weissmann, F. Harnisch, and T. Nakazawa, 2011: The impact of dropwindsonde observations on typhoon track forecasts in DOTSTAR and T-PARC. *Mon. Wea. Rev.*, **139**, 1728–1743, https://doi.org/10.1175/2010MWR3582.1.

Christophersen, H., A. Aksoy, J. Dunion, and S. Aberson, 2018: Composite impact of Global Hawk unmanned aircraft dropwindsondes on tropical cyclone analyses and forecasts. *Mon. Wea. Rev.*, **146**, 2297–2314, https://doi.org/10.1175/MWR-D-17-0304.1.

Cotton, J., and M. Forsythe, 2012: AMVs at the Met Office: Activities to improve their impact in NWP. *Proc. 11th Int. Winds Workshop*, Auckland, New Zealand, EUMETSAT, https://www.eumetsat.int/website/home/News/ConferencesandEvents/DAT_2039311.html.

Ferrier, B. S., Y. Jin, Y. Lin, T. Black, E. Rogers, and G. DiMego, 2002: Implementation of a new grid-scale cloud and precipitation scheme in the NCEP Eta Model. *19th Conf. on Weather Analysis and Forecasting/15th Conf. on Numerical Weather Prediction*, San Antonio, TX, Amer. Meteor. Soc., 10.1, https://ams.confex.com/ams/SLS_WAF_NWP/techprogram/paper_47241.htm.

Goerss, J. S., 2009: Impact of satellite observations on the tropical cyclone track forecasts of the Navy Operational Global Atmospheric Prediction System. *Mon. Wea. Rev.*, **137**, 41–50, https://doi.org/10.1175/2008MWR2601.1.

Gopalakrishnan, S. G., F. Marks Jr., J. A. Zhang, X. Zhang, J.-W. Bao, and V. Tallapragada, 2013: Study of the impacts of vertical diffusion on the structure and intensity of the tropical cyclones using the high-resolution HWRF system. *J. Atmos. Sci.*, **70**, 524–541, https://doi.org/10.1175/JAS-D-11-0340.1.

Grell, G. A., 1993: Prognostic evaluation of assumptions used by cumulus parameterizations. *Mon. Wea. Rev.*, **121**, 764–787, https://doi.org/10.1175/1520-0493(1993)121<0764:PEOAUB>2.0.CO;2.

Heidinger, A., 2010: GOES-R Advanced Baseline Imager (ABI) algorithm theoretical basis document for cloud height. GOES-R Program Office Rep., 77 pp., http://www.goes-r.gov/products/ATBDs/baseline/Cloud_CldHeight_v2.0_no_color.pdf.

Holmlund, K., 1998: The utilization of statistical properties of satellite-derived atmospheric motion vectors to derive quality indicators. *Wea. Forecasting*, **13**, 1093–1105, https://doi.org/10.1175/1520-0434(1998)013<1093:TUOSPO>2.0.CO;2.

Iacono, M. J., J. S. Delamere, E. J. Mlawer, M. W. Shephard, S. A. Clough, and W. D. Collins, 2008: Radiative forcing by long-lived greenhouse gases: Calculations with the AER radiative

transfer models. *J. Geophys. Res.*, **113**, D13103, https://doi.org/10.1029/2008JD009944.

Langland, R. H., C. S. Velden, P. M. Pauley, and H. Berger, 2009: Impact of satellite-derived rapid-scan wind observations on numerical model forecasts of Hurricane Katrina. *Mon. Wea. Rev.*, **137**, 1615–1622, https://doi.org/10.1175/2008MWR2627.1.

Lee, E., Y. Kim, E. Sohn, J. Cotton, and R. Saunders, 2012: Application of hourly COMS AMVs in KMA operation. *Proc. 11th Int. Winds Workshop*, Auckland, New Zealand, EUMETSAT, https://www.eumetsat.int/website/home/News/ConferencesandEvents/DAT_2039311.html.

Le Marshall, J., and L. M. Leslie, 1999: Modelling tropical cyclone intensity. *Aust. Meteor. Mag.*, **48**, 147–152.

——, ——, and A. F. Bennett, 1996a: Tropical Cyclone Beti—An example of the benefits of assimilating hourly satellite wind data. *Aust. Meteor. Mag.*, **45**, 275–279.

——, ——, and C. Spinoso, 1996b: The impact of spatial and temporal distribution of satellite observations on tropical cyclone data assimilation: Preliminary results. *Meteor. Atmos. Phys.*, **60**, 157–163, https://doi.org/10.1007/BF01029792.

——, C. Spinoso, and N. R. Pescod, 1996c: Estimation and assimilation of hourly high spatial resolution wind vectors based on GMS-5 observation. *Aust. Meteor. Mag.*, **45**, 279–284.

——, A. Rea, L. Leslie, R. Seecamp, and M. Dunn, 2004: Error characterization of atmospheric motion vectors. *Aust. Meteor. Mag.*, **53**, 123–131.

——, and Coauthors, 2013: The operational generation of continuous winds in the Australian region and their assimilation with 4DVAR. *Wea. Forecasting*, **28**, 504–514, https://doi.org/10.1175/WAF-D-12-00018.1.

Leslie, L. M., J. F. Le Marshall, R. P. Morison, C. Spinoso, R. J. Purser, N. Pescod, and R. Seecamp, 1998: Improved hurricane track forecasting from the continuous assimilation of high quality satellite wind data. *Mon. Wea. Rev.*, **126**, 1248–1257, https://doi.org/10.1175/1520-0493(1998)126<1248:IHTFFT>2.0.CO;2.

Lu, X., X. Wang, M. Tong, and V. Tallapragada, 2017: GSI-based, continuously cycled, dual-resolution hybrid ensemble-variational data assimilation system for HWRF: System description and experiments with Edouard (2014). *Mon. Wea. Rev.*, **145**, 4877–4898, https://doi.org/10.1175/MWR-D-17-0068.1.

Menzel, W. P., 2001: Cloud tracking with satellite imagery: From the pioneering work of Ted Fujita to the present. *Bull. Amer. Meteor. Soc.*, **82**, 33–47, https://doi.org/10.1175/1520-0477(2001)082<0033:CTWSIF>2.3.CO;2.

Mitchell, K., 2005: The community Noah Land Surface Model (LSM). NOAA/NCEP/EMC Rep., 26 pp., https://ral.ucar.edu/sites/default/files/public/product-tool/unified-noah-lsm/Noah_LSM_USERGUIDE_2.7.1.pdf.

Nieman, S. J., W. P. Menzel, C. M. Hayden, D. Gray, S. Wanzong, and J. Daniels, 1997: Fully automated cloud-drift winds in NESDIS operations. *Bull. Amer. Meteor. Soc.*, **78**, 1121–1133, https://doi.org/10.1175/1520-0477(1997)078<1121:FACDWI>2.0.CO;2.

Rogers, E., T. Black, B. Ferrier, Y. Lin, D. Parrish, and G. DiMego, 2001: Changes to the NCEP Meso Eta Analysis and Forecast System: Increase in resolution, new cloud microphysics, modified precipitation assimilation, modified 3DVAR analysis. NOAA/NCEP/EMC Tech. Procedures Bull., http://www.emc.ncep.noaa.gov/mmb/mmbpll/mesoimpl/eta22tpb/.

Su, X., J. Daniels, J. Derber, Y. Lin, A. Bailey, W. Bresky, and H. Qi, 2014: Assimilation of GOES hourly AMVs in NCEP global data assimilation and forecast system. *Proc. 12th Int. Winds Workshop*, Copenhagen, Denmark, EUMETSAT, https://www.eumetsat.int/website/home/News/ConferencesandEvents/DAT_2441511.html?lang=EN.

Tallapragada, V., C. Kieu, Y. Kwon, S. Trahan, Q. Liu, Z. Zhang, and I. Kwon, 2014: Evaluation of storm structure from the operational HWRF model during 2012 implementation. *Mon. Wea. Rev.*, **142**, 4308–4325, https://doi.org/10.1175/MWR-D-13-00010.1.

Tong, M., J. Sippel, V. Tallapragada, E. Liu, C. Kieu, I. Kwon, W. Wang, Q. Liu, Y. Ling, and B. Zhang, 2018: Impact of assimilating aircraft reconnaissance observations on tropical cyclone initialization and prediction using operational HWRF and GSI ensemble–variational hybrid data assimilation. *Mon. Wea. Rev.*, **146**, 4155–4177, https://doi.org/10.1175/MWR-D-17-0380.1.

Velden, C. S., and S. B. Goldenberg, 1987: The inclusion of high density satellite wind information in a barotropic hurricane-track forecast model. Preprints, *17th Conf. on Hurricanes and Tropical Meteorology*, Miami, FL, Amer. Meteor. Soc., 90–93.

——, C. M. Hayden, M. S. J. Nieman, W. P. Menzel, S. Wanzong, and J. S. Goerss, 1997: Upper-tropospheric winds derived from geostationary satellite water vapor observations. *Bull. Amer. Meteor. Soc.*, **78**, 173–195, https://doi.org/10.1175/1520-0477(1997)078<0173:UTWDFG>2.0.CO;2.

——, and Coauthors, 2005: Recent innovations in deriving tropospheric winds from meteorological satellites. *Bull. Amer. Meteor. Soc.*, **86**, 205–223, https://doi.org/10.1175/BAMS-86-2-205.

——, W. E. Lewis, W. Bresky, D. Stettner, J. Daniels, and S. Wanzong, 2017: Assimilation of high-resolution satellite-derived atmospheric motion vectors: Impact on HWRF forecasts of tropical cyclone track and intensity. *Mon. Wea. Rev.*, **145**, 1107–1125, https://doi.org/10.1175/MWR-D-16-0229.1.

Wang, X., D. Parrish, D. Kleist, and J. Whitaker, 2013: GSI 3DVar-based ensemble–variational hybrid data assimilation for NCEP Global Forecast System: Single-resolution experiments. *Mon. Wea. Rev.*, **141**, 4098–4117, https://doi.org/10.1175/MWR-D-12-00141.1.